SAND2023-05275T

THESIS

CHARACHTERIZATION OF PLASMA CONDUCTIVITY BY LASER THOMSON SCATTERING IN A HIGH-VOLTAGE LASER-TRIGGERED SWITCH

Submitted by

Jacob A. Gottfried

Department of Mechanical Engineering

In partial fulfillment of the requirements

For the Degree of Master of Science

Colorado State University

Fort Collins, Colorado

Summer 2023

Master's Committee

Advisor: Azer P. Yalin

Ciprian Dumitrache

Jorge Rocca

SAND2023-##### T

Colorado State University acknowledges funding support from Sandia National Laboratories. Sandia National Laboratories is a multi-mission laboratory managed and operated by National Technology & Engineering Solutions of Sandia, LLC, a wholly owned subsidiary of Honeywell International, Inc., for the U.S. Department of Energy's National Nuclear Security Administration under contract DE-NA0003525.

This paper describes objective technical results and analysis. Any subjective views or opinions that might be expressed in the paper do not necessarily represent the views of the U.S. Department of Energy or the United States Government

ABSTRACT

CHARACHTERIZATION OF PLASMA CONDUCTIVITY BY LASER THOMSON SCATTERING IN A HIGH-VOLTAGE LASER-TRIGGERED SWITCH

High-voltage laser-triggered switches (HV-LTSs) are used in pulsed-power applications where low jitter and precise timing are required. The switches allow operation in the megaampere, megavolt regime while maintaining low insertion losses. Low inductance HV-LTS designs have shown discrepancies between modeled and experimental behavior, reinvigorating interest in the physics of HV-LTS operation. Detailed spatially- and temporally- resolved measurements of plasma properties within the switches could contribute to validating and advancing numeric models of these systems by checking the assumptions used in their derivation. To date, there is minimal experimental data detailing the evolution of plasma properties during switch operation.

This thesis investigates HV-LTS plasma channel conductivity (the assumption within current models drawing the most critique) during the rising edge of the current pulse through both derivative (V-Dot) electrical probes and electron temperature measurements via laser Thomson scattering. A HV-LTS testbed utilizing an aqueous (variable impedance) resistive load was designed to produce experimental conditions found in larger pulsed power applications. This paper describes the design of the load and experimental results under a variety of load conditions and operating voltages of 5 - 6 kV. The results indicate the electron temperature increases during the rising edge of the current pulse, suggesting that the plasma conductivity is temporally evolving. Further, electrical measurements show an increase in plasma conductivity during the rising edge

of the current pulse. Evidence from both optical and electrical measurements calls into question the assumption of a temporally constant plasma conductivity as both the optical and electrical diagnostics show a temporally increasing plasma conductivity.

Table of Contents

LIST OF FIGURES

List of Tables

CHAPTER 1: INTRODUCTION

1.1 Current State of Pulsed Power Research

Pulsed Power is an active field of research designed to study high energy density physics at conditions similar to those that occur in stars and during the detonation of atomic weapons. To safely generate these conditions on Earth, electric pulses are used. These electric pulses consist of megavolt potentials and megaampere currents in pulses on the order of milliseconds down to tens on nanoseconds. These pulses are generated by amassing electrical energy by slowly charging the primary energy storage stage. Where primary energy storage is often arranged in a Marx bank (capacitive) configuration [1] to deliver large currents in short (microsecond) time spans. The stored energy is then rapidly discharged into a load using high-power switches. One example of this is the Z-machine developed by Sandia National Laboratory which is the world's most powerful radiation source.

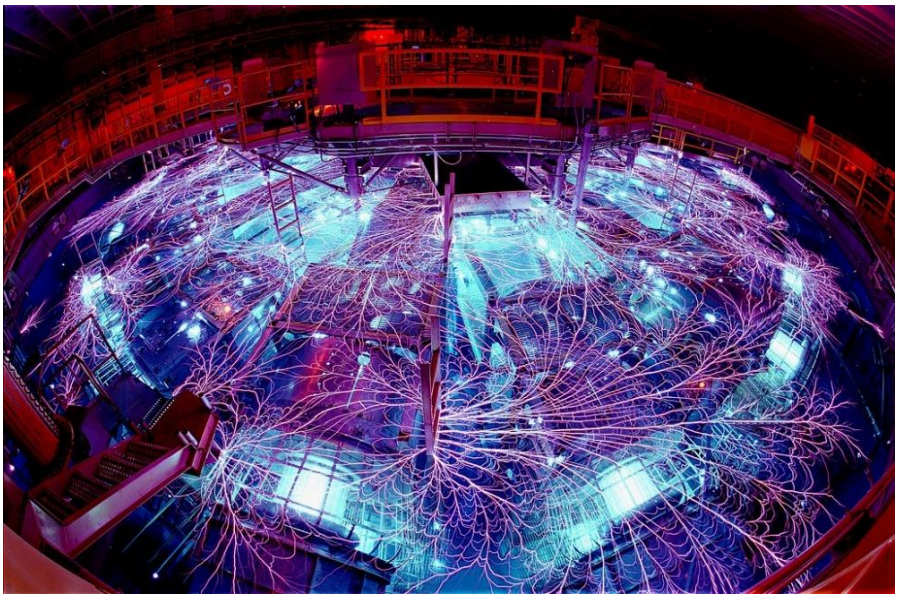

Figure 1-1 Sandia National Laboratories Z - machine. Credit: https://www.sandia.gov/z-machine

There are a variety of closure mechanisms used for spark-gap switches in pulsed power research such as self-break [2], pulsed charging [3], field distortion [4–6], and laser-triggering [7–11]. Out of the closure mechanisms, laser-triggering has become the prominent option for pulsed power research due to a variety of benefits [12]. For example, High-Voltage Laser-Triggered Switches (HV-LTSs) have low temporal jitter in closure time, allowing for tens to possibly hundreds of HV-LTSs to be triggered simultaneously [7,12–16]. Furthermore, the laser energy required for switch closure is typically less than 20 mJ, allowing for a single laser pulse to be fiber delivered to several switches, further decreasing temporal jitter between switches, and lowering the cost per-switch.

1.2 High-Voltage Laser-Triggered Switch Operation

One of the earliest uses of lasers, was for the laser triggering of spark gap switches [7,17,10]. Through laser triggering, the current flow is guided by the laser, leading to a single uniform plasma

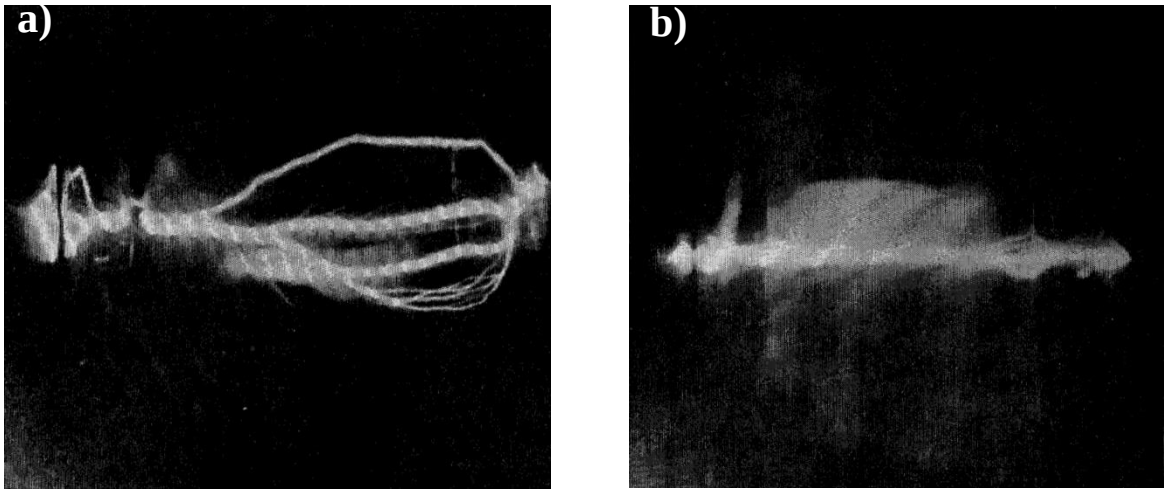

Figure 1-2 Copywrite Guenther, A. Bettis, J. 1967. A) Megavolt spark-gap switch mechanically/electrically triggered. B) Megavolt switch laser triggered.

channel rather than the several streamers seen from mechanical or electrical switching as depicted in figure 1.1.2 [7,14,17].

In pulsed power applications, HV-LTS often sit between primary energy storage and the pulse forming network in large pulsed-power machines [18] facilitating both pulse compression and precise timing [19]. The basic design of a high-voltage laser-triggered switch includes two electrodes positioned a distance on the order millimeters to centimeters from each other and sealed within a chamber that can be pressurized to allow for high voltages without an electrical breakdown of the gas. The working gas and pressure are typically selected such that the electric potential difference between the electrodes 15 – 25% below the self-breakdown voltage [12,14–16,20–23]. To close the switch an intense laser pulse focused at the center (or less effectively on one) of the electrodes resulting in a plasma kernel [13]. This kernel expands for the duration of the laser pulse forming a plasma mid gap. Often the laser pulse width is shorter than the switch run time (change in time from laser pulse to meaningful current flow). Following a decrease in laser energy the plasma's electron temperature and density (of the laser induced plasma) are observed to temporarily decrease while expanding both radially and axially [11,21,24]. Given the plasma channel is conductive and mid gap, the externally applied electric field stress is dramatically increased such that streamers propagate connecting the electrodes resulting in a highly conductive path allowing meaningful current to flow [22].

1.3 Relevant Plasma Physics

Plasmas are a state of matter consisting of two major components: an ionized gas and the associated freed electrons. Due to the free electrons, plasmas respond to external stimuli from both electric and magnetic fields, making plasmas controllable. To date, plasmas are found in both

scientific and commercial applications ranging from light sources and display technology [25–27], semiconductor manufacturing [28], advanced coating application [29], and space propulsion [30,31] to nuclear fusion [32], and high power switches [16,20].

An important property of plasmas is their quasi-neutrality which is defined as an even charge distribution resulting in a net neutral charge when individual particle charges are summed over an arbitrary volume [33]. As external electric fields are applied to plasmas, the charges will begin to separate, however, this separation induces internal electric fields which work to counteract the external forces and re-establish quasi-neutrality. This balance of forces leads to a maximum electromagnetic wavelength that a given plasma can shield itself from. This relationship is described as the Debye radius :

$$\lambda_D = \sqrt{\frac{\varepsilon_0 k_B T_e}{n_e e^2}} \tag{1.3.1}$$

where T_e is the *plasma electron temperature* and n_e is the *density of free electrons*. The Debye radius can be intuitively understood as the characteristic length over which the plasma can shield itself from external forces. Therefore, any electromagnetic wave with a wavelength greater than the Debye radius will interact with electrons acting in a collective nature while electromagnetic waves with a wavelength less than the Debye radius will interact with individual electrons. An important note about the Debye radius, as presented in equation 1.3.1, is that the plasma is assumed to be "cold" (T_e < 100 eV) meaning that there is insufficient kinetic energy for ion transport to be relevant at the time scales of interaction.

An additional property of plasmas that is utilized in the development of high-voltage switches is the low electrical resistivity of plasmas. The general expression for conductivity of a plasma is given as [34]:

$$\sigma_P = \frac{\epsilon_0 \omega_{pe}^2}{i\omega + \nu_m} \tag{1.3.2}$$

where ω_{pe} is the *plasma frequency*, ω is the *frequency of the driving electric field,* and ν_m is the *collisional frequency*. A more applicable case for the plasma conductivity equation is the dc plasma conductivity equation [34,35]:

$$\sigma_{dc} = \frac{e^2 n_e}{m \upsilon_m} \tag{1.3.3}$$

where e is the *electron number density* and υ_m is the electron-neutral collision frequency. To arrive at the form of equation (1.3.3), two major assumptions are required including that $\omega \ll \upsilon_m$ and that there is a low degree of ionization (the cold plasma approximation) [34].

On the other extreme, one has the case where the plasma reaches a high degree of ionization allowing for the assumption that all electrical momentum transfer occurs due to far range Coulomb collisions and that contributions due to neutral particles can be ignored [36,39–41]. The model used in this case is referred to as the Spitzer resistivity and is the form used in current HV-LTS models [9,36,37]:

$$\eta = \frac{2\sqrt{2\pi}}{3} \frac{Ze^2 \sqrt{m_e} \ln \Lambda}{(4\pi\varepsilon_0)^2 (k_B T_e)^{3/2}} = \frac{1}{\sigma} \tag{1.3.4}$$

where Z is the *degree of ionization*, e and m_e are the *elemental charge and mass*, ε_0 is the *electric permittivity*, k_B is the *Boltzmann constant*, T_e is the plasma electron temperature, and Λ is the *Coulomb logarithm* defined by [33,38] :

$$\ln \Lambda = \frac{\lambda_D}{r_\perp} = 12\pi n_e \lambda_D^3 \tag{1.3.5}$$

where λ_D is the *Debye radius* of the plasma and $r_\perp$ is the *minimum radius of the Coulomb collision*.

1.4 Motivation: The Martin and Braginskii Models

To understand the physics of pulsed power systems, an accurate model of switch operation and power delivery is essential. This, along with the complex nature of plasma channel growth in HV-LTS's, has led to significant research modeling their plasma channel evolution [3,9,15,20,22,42,43]. The theory of plasma channel development in HV-LTS began with Braginskii's work to characterize plasma channel development in high pressure and under moderate current (with an example being lightning) [42]. In this work, Braginskii used the analogy that during the rising edge (and plateauing) of the current flow through the plasma, the plasma can be treated as a radially expanding cylinder with an attached blast wave that acts as a piston [3,42]. The shock front remains attached to plasma channel until the current decreases, allowing the plasma to cool [42]. In this analogy, the moving piston heats and ionizes the surrounding gas leaving a low density (relative to the bulk gas) region that is occupied by the conducting plasma [3,42]. The major result of Braginskii's work is referred to as the Braginskii model power balance [42]:

$$\frac{I}{\sigma} = 2\pi^2 \rho_0 (rr')^2 \xi \tag{1.4.1}$$

where I is the *current*, σ is *plasma conductivity*, ρ_0 is *neutral gas density*, r and r' is *plasma radius and its time derivative*, and ξ is a *dimensionless constant* given by:

$$\xi = K_p \left[1 + \frac{2}{3(\gamma-1)}\right] \tag{1.4.2}$$

where Kp is the *coefficient of resistance constant* (.9) [3], and γ is the *ratio of specific heats* (1.4) in dry room air.

This power balance states that, during the current-rise phase, it is assumed the effects of Joule heating within the plasma are canceled by the energy required for the shockwave and ionization, resulting in constant plasma conductivity (and in turn constant T_e) [3,14,21,42]. Additionally, Braginskii assumed that the radial growth of the plasma channel has the power form:

$$r(t) = At^k \tag{1.4.3}$$

However, this has been empirically verified to be an accurate assumption [9,14,44]. An important note about the Braginskii model power balance is a lack of spatial or temporal dependence for several parameters, including the plasma conductivity (as shown in equation 1.4.1), which will be specifically investigated in this thesis.

The work of Braginskii was further expanded by Tom Martin to quantify the energy loss mechanisms in high-voltage spark-gap switches [3]. Martin brought equation (1.4.1) into the time domain by solving the power balance for time-dependent current. The result is an equation for the time varying plasma channel radius [3]:

$$r^2(t) = \left(\frac{4}{\pi^2 \rho_0 \xi \sigma}\right)^{\frac{1}{3}} \int_0^t I^{\frac{2}{3}} dt \tag{1.4.4}$$

It was then assumed that the major energy loss mechanism in the switch is resistive losses within plasma channel. From equation (1.4.4), the plasma channel resistance is calculated through [3]:

$$R = \frac{L}{\sigma \pi r^2} \tag{1.4.5}$$

where L is the spark gap length. Again, it was assumed that the plasma channel conductivity is neither a function of plasma channel radius nor time as evidenced by its removal from the integral in equation (1.4.4).

To calculate the energy loss, the plasma channel conductivity is required. As stated in section 1.3, HV-LTSs are assumed to operate in a regime where the Spitzer conductivity model applies and therefore equations (1.3.4) and (1.3.5) are used to calculate the electrical conductivity in equation (1.4.5). From equation (1.3.4), it is evident that plasma conductivity is a function of electron temperature. Therefore, the resistance (and energy loss in the switch) are functions of the plasma electron temperature.

Ultimately, Tom Martin's model has become the most popular model for HV-LTS's in pulsed power applications and is the model used for transmission line simulation programs for pulsed power systems, like BERTHA [15]. For a large range of switches, this model accurately simulated their behavior [3,22,42,45]. However, these switches typically contained a large inductive component and long current pulses (order microseconds to milliseconds). Under these operating conditions, the current pulse takes the form of a square wave where the current rise and fall times are significantly shorter than the switch on time (allowing for stabilization of plasma channel properties).

Due to the large power densities delivered by these switches, energy losses of a few percent can be on the order of megawatts or more. This has led to a constant drive to reduce these insertion losses, leading to significant interest in lowering the inductive components of the switches. However, as new modern (low inductance) switches have been developed, failures of the Martin/Braginskii model have become apparent. Specifically, the Martin/Braginskii model is under-predicting current rise times and over predicting current on times [15]. The suspected reason for the observed discrepancy is the assumption that transient plasma properties are small by comparison and behavior is dominated by stable plasma characteristics, namely conductivity. Given these assumptions, it is clear to see why this model is largely accurate for higher inductance systems. In turn, it is apparent that as the current pulse's on-time is shortened such that it is on the order of the turn on time, the transient's matter and the Martin/Braginkii model breaks down. This regime of low inductance switches with current pulses on the order of hundreds of nanoseconds is highly sought after for pulsed power applications and reinvigorating this area of research and motivating this thesis to measure the plasma channel conductivity and empirically show the breakdown of the Martin/Braginskii model [11,44].

1.5 Laser Scattering as a Diagnostic

1.5.1 Rayleigh and Raman Scattering

As light travels through any medium, the photons interact with particles, molecules, and atoms that comprise the medium. Depending on the ratio of objects size to wavelength of the light, one of several scattering mechanisms occur. The dominant form of laser scattering from neutral particles is elastic scattering which occurs for both particles larger than lasers wavelength, such as dust (Mie scattering) and smaller than the lasers wavelength, such as atomic or molecular species

(Rayleigh scattering). Elastic scattering, as the name implies, does not change the energy of the scattered photon and therefore, appears at the same wavelength as the incident laser light. Elastic scattering can provide information about neutral particle size or number density in a variety of applications. However, in this work, the strong magnitude of elastic scattering presents a significant concern for both safety of detection equipment and overshadowing of relevant scattering mechanisms (the scattering cross-section for Rayleigh scattering is approximately 1000 times stronger than Raman scattering in air [46]). The magnitude of elastic scattering is compared against Rotational Raman Scattering in figure 1-3.

The weaker scattering mechanism is inelastic scattering, specifically Raman scattering, which occurs for molecules that experience a change in molecular polarizability between rotational or

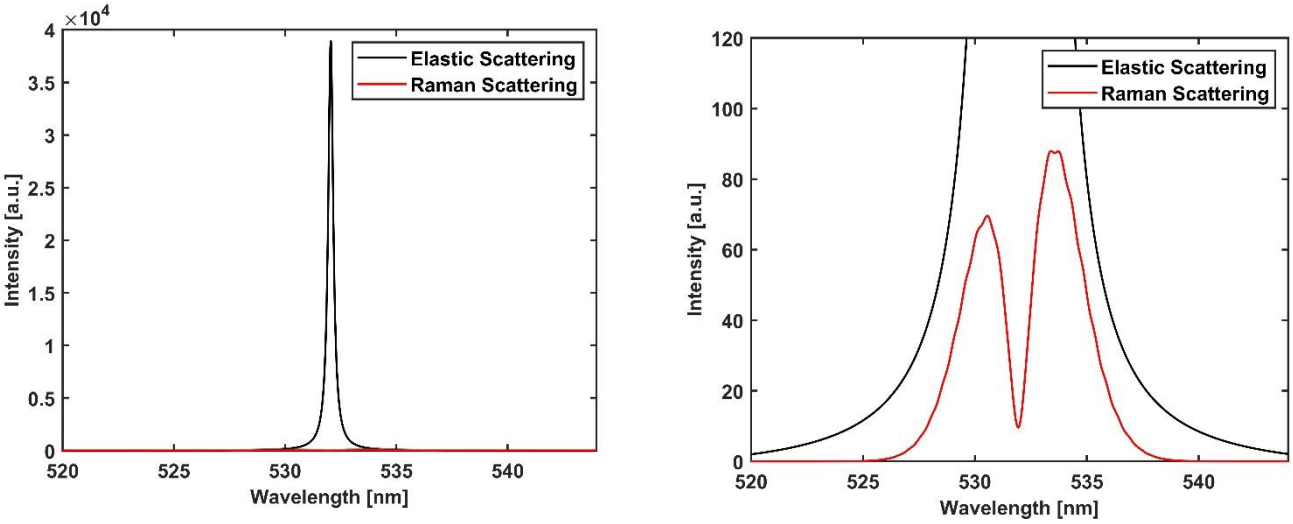

Figure 1-3 Left: Full scale comparison of elastic and Raman scattering. Right) Zoomed in version of left plot

vibrational states. The specific case of interest in this work is spontaneous Rotational Raman Scattering as it provides a useful mechanism for calibrating detection equipment.

In rotational Raman scattering, a molecule absorbs a photon of incident laser light, exciting it to a higher rotational state. Following the excitation, the molecule will spontaneously emit a

photon as it drops to a lower energy state [47]. The molecule can drop to a higher energy state than it was originally at resulting in an emitted photon of a longer wavelength than absorbed (the Stokes S branch) or a lower energy level, emitting a shorter wavelength photon than absorbed (the anti-Stokes P branch) [47]. The energy shifts as well as the ratio of scattering power between energy shifts provides the distribution of rotational energy levels and in turn, information about the bulk gas temperature.

The wavelengths associated with rotational energy level shifts are [48]:

$$\lambda_{J\to J+2} = \lambda_i + \frac{\lambda_i^2}{hc} \cdot B(4J+6) \tag{1.5.1}$$

for the Stokes S branch and

$$\lambda_{J\to J-2} = \lambda_i - \frac{\lambda_i^2}{hc} \cdot B(4J-2) \tag{1.5.2}$$

for the anti-Stokes P branch where λ_i is the *incident laser wavelength*, J is the *rotational quantum number*, and B is the *rotational constant of the molecule*. The given power of an individual peak is given by [48] :

$$P_{J\to J'} = P_i n_J L_{det} \frac{d\sigma_{J\to J'}}{d\Omega} \Delta\Omega \tag{1.5.3}$$

where n_J is the *density of the initial rotational state, J* and P_i is the *power of the incident laser radiation* and $\Delta\Omega$ is the *collection solid angle*. For a 90 degree collection angle and assuming the incident laser radiation is polarized in the collection direction, the differential cross section for a Raman transition $J \to J'$ can be written in terms of the polarizability tensor, γ, as [48]

$$\frac{d\sigma_{J\to J',\perp}}{d\Omega} = \frac{64\pi^4}{45\varepsilon_0^2} \cdot b_{J\to J'} \cdot \frac{\gamma^2}{\lambda_{J\to J'}^4} \quad (1.5.4)$$

where $b_{J\to J'}$ is the Placzek-Teller coefficients given by [47,48]

$$b_{J\to J+2} = \frac{3(J+1)(J+2)}{2(2J+1)(2J+3)} \quad (1.5.5)$$

$$b_{J\to J-2} = \frac{3(J-1)}{2(2J+1)(2J-1)} \quad (1.5.6)$$

1.5.2 Thomson Scattering

Laser Thomson scattering was originally developed for nuclear fusion applications in the 1960s [49]. Since then, Thomson scattering has been applied over a broad range of both electron temperature (~0.1–10 eV) and density (~10^{13}-10^{20} cm^{-3}) [21,24,50–55] and pulse rates up to 10 kHz [56]. Laser Thomson Scattering is dipole radiation due to the acceleration of charged particles, predominantly from free electrons due to their small mass [21,24,53]. The broadening and overall scattering spectral form factor of laser Thomson Scattering is produced by Doppler shifting of the incident laser light, including possible collective effects, with respect to both the electron and the observer [24,48,57].

Due to the mostly free motions of the electrons in the plasma, the individual scattered photons add up such that the spectrum is representative of the Electron Energy Distribution Function (EEDF) of the plasma [24]. Therefore, one can directly determine both the plasma's electron temperature and density without any assumptions concerning equilibrium conditions of the plasma. For the calculations in this work, the electron energy distribution function (EEDF) is

assumed to be a pure Maxwellian, an assumption that is commonly used for similar laser and electrically induced plasmas [24,53,58].

The spectrum produced by laser Thomson scattering takes one of two forms depending on the way the incident laser light interacts with the electrons in the plasma. As discussed in section 1.3, an electromagnetic wave can interact with either shielded or individual electrons. In the context of Thomson scattering, the degree of shielding is described by the scattering parameter, α. Originally introduced by Salpeter, the scattering parameter governs the shape of the LTS spectrum [24,48,59]:

$$\alpha \equiv \sqrt{\frac{n_e e^2}{T_e k_B \varepsilon_0 k^2}} = \frac{1}{k\lambda_D} = \frac{\lambda_L}{sin\left(\frac{\Theta}{2}\right)}\sqrt{\frac{n_e}{T_e}} \qquad (1.5.7)$$

where k_B is the *Boltzmann constant*, ε_0 is *vacuum permittivity of free space*, k is the *wavenumber of the incident light* determined by angle θ, as depicted in figure 1-4 (left). Two limiting regimes occur when $\alpha << 1$, for which the scattering is described as non-collective, meaning scattering mostly results from individual electrons, and when $\alpha >> 1$, for which the scattering is described as collective, meaning scattering mostly results from shielded electrons [24,55].

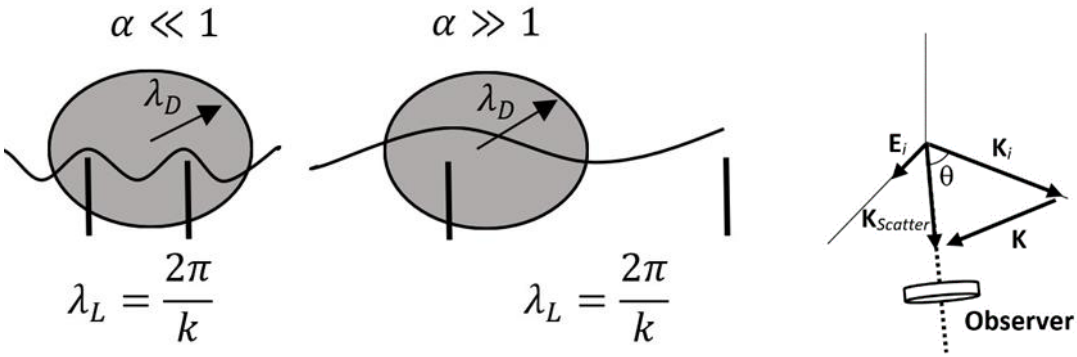

Figure 1-4 Left) Comparison of incident laser wavelength and plasma Debye radius. Right) Dependence of collection angle where Ki and Ei are the propagation and polarization vectors for the incident laser, Kscatter is the collection vector, and K is the change in direction.

Non-collective scattering is the result of scattering taking place with optical wavelength much smaller than λ_D [24]. Since the scattering is occurs from interactions with individual electrons, the velocity of the electrons is approximately random (with respect to the laser direction and observer) allowing the partial scattered waves to sum into a form representative of the EEDF [24]. If the EEDF is Maxwellian, the scattering spectra is a Gaussian distribution centered around the incident laser wavelength, as depicted in figure 1-5 [48]. The electron temperature, T_e, is determined from the width of the Gaussian distribution and the electron density, n_e, is determined by the total integrated scattering power [48]. Since the integrated area is needed to determine n_e, the value of the total scattering power must be calibrated [24,48,60]. The typical methods for calibrating the scattering power is via rotational Raman scattering from neutral molecules [24,48], as rotational Raman scattering is reliable simulated if the density, composition, and temperature of the gas is known.

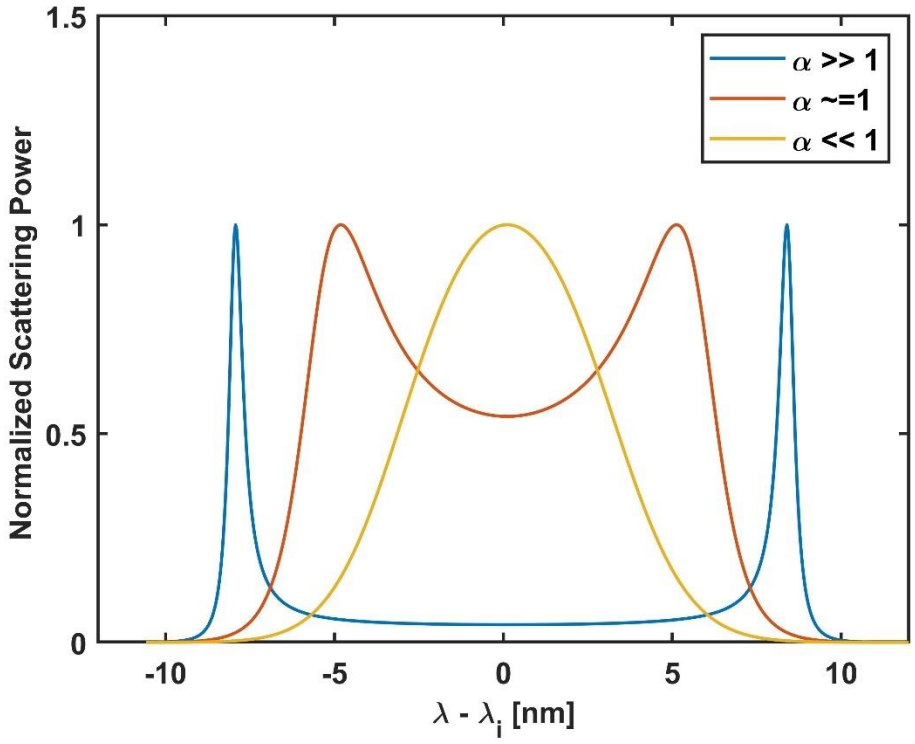

Figure 1-5: Change in Thomson Scattering (electron) Form Factor equation based on different alpha values.

In a plasma, electrons are not truly free to move but are subject to weak electric fields within their Debye radius. When scattering occurs over an optical wavelength similar to or greater than the Debye length, the incident laser wavelength interacts with the shielded electrons, leading to collective scattering [24,48]. In collective Thomson Scattering, four distinct peaks are observed in the spectrum where two correspond to electron contributions and two correspond to ionic contribution. In the case of collective scattering, the shape (not area) of the satellite peaks is a function of the plasma electron or ion temperature through the Thomson Scattering from factor [24,48]. Assuming the electron energy distribution function (EEDF) is Maxwellian [24,53,58] and the Salpeter approximation applies, the Thomson scattering form factor, $S(\boldsymbol{k}, \omega)$, is [57,59]:

$$S(\boldsymbol{k},\omega) \approx \frac{\sqrt{2\pi}}{\nu_{te}}\Gamma_{\alpha}(\xi_e) + \frac{\sqrt{2\pi}}{\nu_{ti}}\left[\frac{1}{(k\lambda_D)^2+1}\right]^2 \Gamma_{\beta}(\xi_i) \tag{1.5.8}$$

where the line shape functions, Γ_{α}, and Γ_{β} , are [54]:

$$\Gamma_{\alpha}(\xi_e) = \frac{\exp(-{\xi_e}^2)}{|1+\alpha^2 w(\xi_e)|^2} \qquad \Gamma_{\beta}(\xi_i) = \frac{\exp(-{\xi_i}^2)}{|1+\beta^2 w(\xi_i)|^2} \tag{1.5.9}$$

where the scattering parameters, α and β, are [54],

$$\alpha^2 = \frac{1}{(k\lambda_D)^2} \qquad \beta^2 = \left[\frac{1}{(k\lambda_D)^2+1}\right]\frac{ZT_e}{T_i} \tag{1.5.10}$$

where the plasma dispersion function, w(ξ), is [61]

$$w(\xi) = 1 - 2\xi_j e^{-{\xi_j}^2}\int_0^{\xi_j} e^{-\zeta^2} d\zeta + i\pi^{\frac{1}{2}}\xi_j e^{-{\xi_j}^2} \tag{1.5.11}$$

where the ratio, ξ_j, of wave phase velocity to the element thermal velocity is [61]:

$$\xi_j = \frac{\omega}{k\nu_{tj}\sqrt{2}} \tag{1.5.12}$$

and the element thermal velocity, ν_{tj} is:

$$\nu_{tj} = \sqrt{\frac{8k_B T_j}{\pi m_j}} \tag{1.5.13}$$

where index j can be either e or i for the electron and ionic contributions respectively. However, in application, the large mass of the ions results in a low ion thermal velocity and in turn, small frequency shift leading to challenges spectrally resolving the ionic contribution from laser line scattering. For this work, the ionic contribution of equation (1.5.8) will not be considered.

Therefore, the final form of the Thomson scattering form factor is a function of T_e, allowing for the electron temperature to be determined from measured laser Thomson Scattering spectra. In addition to electron temperature, the electron density can also be determined from the wavelength separation of the (electron) satellite peaks $\Delta\omega_e$ [24]:

$$\Delta\omega_e = \pm\left(\frac{e^2 n_e}{\varepsilon_0 m_e} + \frac{3k_B T_e k^2}{m_e}\right)^{\frac{1}{2}} \quad (1.5.14)$$

1.6 Thesis Objectives and Outline

The main objectives of this thesis are to evaluate the assumption in the Martin/Braginskii model of a temporally constant plasma conductivity during the operation of a high-voltage laser-triggered switch. The layout of the remainder of this paper is as follows:

- Develop a variable impedance load for a high-voltage laser-triggered switch
- Develop a laser Thomson scattering system capable of measuring the plasma characteristics during the rising edge of the current pulse
    - The system must be non-perturbative to switch operation
    - A temporal resolution of 10 ns is required to inform current numerical models
- Develop an electrical diagnostic system to measure voltage drop across the electrodes
- Compute and compare the plasma conductivity from the two diagnostics to gain insight into the evolution of the plasma channel conductivity.

CHAPTER 2: HV-LTS TEST STAND

2.1 Previous Work

The theory of High-Voltage Laser-Triggered Switches (HV-LTS) described in section 1.4 shows a predicted breakdown of the Martin/Braginskii model for switches operating with low inductance circuits. This motivated the development of a HV-LTS testbed at Colorado State University that operated a 200 kV class switch with a lumped circuit impedance of 90 mH [14]. Figure 2-1 was the circuit used for the low inductance switch testbed. To achieve the high voltage while maintaining a low resistance, the main energy storage consisted of two 20 nF, 100 kV capacitors (with an equivalent series inductance, ESI, of 180 mH) in parallel.

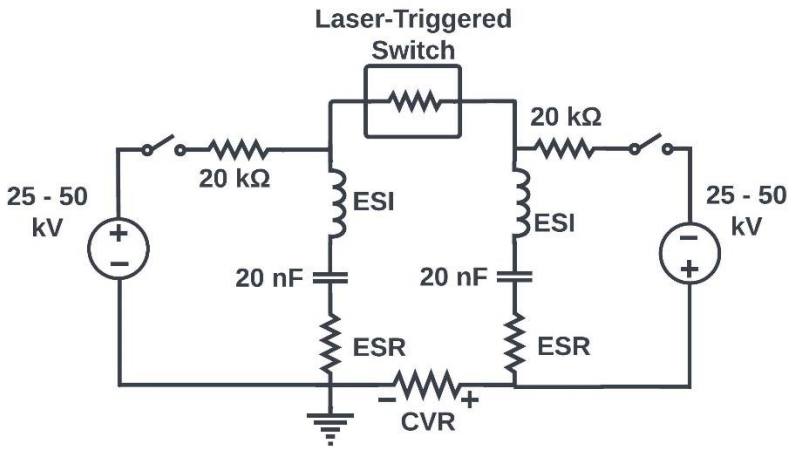

Figure 2-1 Short Circuit electrical configuration used in previous work.

Although this circuit allowed for testing a high-voltage, low-inductance switch condition, it effectively resulted in a short-circuit configuration after the initial switch closure. Due to the short circuit, the current was observed to ring between the capacitors throughout the duration of switch

operation [14,21]. This condition is not representative of a pulse power application which have current delivered to a load with minimal current reflection [62].

2.2 Electrical Circuit

To operate under conditions relevant to pulsed power applications (minimal current reflection), the previous electrical circuit was modified. Figure 2-2 is the electrical diagram for the modified switch test bed used in this work. For the modified circuit, primary energy storage is a single 20 nF, 100 kV capacitor. The second capacitor was replaced by a high-power variable impedance load, raising the circuit lumped impedance to ~ 200 mH but removing reflection in the current.

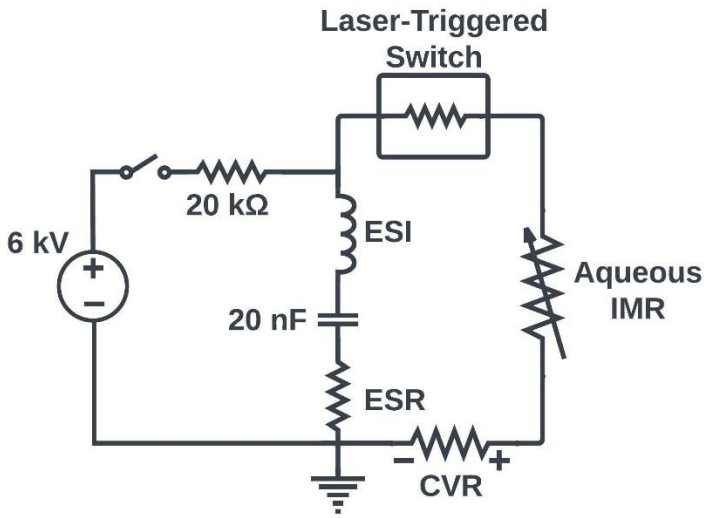

Figure 2-2 HV-LTS circuit with resistive load. ESI and ESR refer to equivalent series inductance and resistance respectively, CVR refers to current viewing resistor, and IMR stands for impedance matching resistor.

The charge/operation of the circuit is controlled by an external programable control circuit [14] and consists of a gas purge/charge, isolation, and operation phase. During the gas

purge/charge phase, a 20 PSI purge flow of ultra-zero dry air is injected into the switch housing for a period of two seconds. The purge flow removes any change in gas composition caused by the pervious laser-induced or electrically-induced plasma. The exchange of the switch working gas is important as a pulsed power application typically consists of a single shot and therefore, the working gas in the switch should have unmodified properties prior to each new shot. While the purge flow is on, an energizing relay (Ross 40 kV-air) connects a 125 kV DC power supply (Glassman WK series PS/WK125P5.0-11) to the capacitor. The power supply current is set such that the capacitor reaches its intended voltage during the purge flow duration. As a safety measure, a 20 kΩ copper sulfate (CuSO4) liquid charge resistor is added between the relay and capacitor. This protects the room electronics in the case of an accidental switch closure (electrical self-break caused excessive applied voltage). After the purge/charge phase the energizing relay is opened, isolating the switch. The isolation phase consists of the time required to actuate the relay and send a signal to a delay generator controlling the lasers and collection electronics. Due to parasitic losses from the capacitor to ground during the isolation phase leading to unaccounted error in voltage measurements, it is ideal to minimize this phase. With the current timing circuits, the isolation phase is set to 0.5 seconds to ensure the relays have fully actuated.

2.3 Switch Laser-Triggering

The HV-LTS used in this work was developed by Sandia National Laboratories for operation at high pressures (10 – 20 bar) and voltages up to 200 kV. Figure 2-3 is a cartoon graphic of the switch internal geometry. The switch consists of two electrodes with a 3.5-millimeter spark gap where the electrode diameter is an order of magnitude greater than the gap, allowing for the internal electric field to be modeled as parallel plates. The switch housing has been modified to

allow optical access on two orthogonal axes. In previous work, these access ports were sealed with windows allow the system to be pressurized [14,22]. However, the optical diagnostics used in this thesis are highly sensitive elastic scattering of laser light and the windows used in pervious switch housing designs scattered light to a prohibitive degree, requiring their removal. Without windows, the switch is limited to operation at ambient pressure and temperature lowering the maximum operating voltage to ~ 7.5 kV [63]. Due to this limitation, the switch is operated at voltages of 5 and 6 kV resulting in self-break percentages between 65 – 80%.

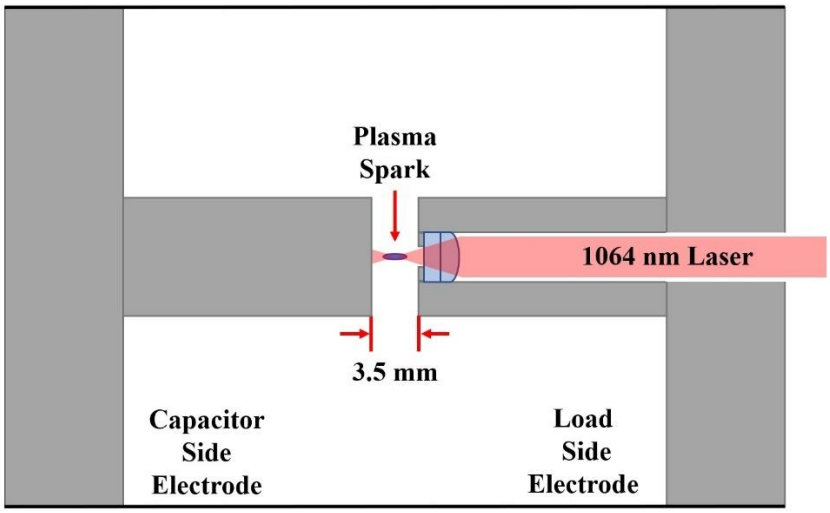

Figure 2-3 Cartoon of HV-LTS switch geometry.

The switch is triggered by a single 14 mJ, 12 ns FWHM pulse from the 1064 nm output of a Nd:YAG laser (Quantel Big Sky) that is approximately 4 mm diameter. The laser pulse enters the switch through an optical access port in the load-side electrode. A focusing lens mounted within the load-side electrode brings the laser pulse to a tight waist, generating a sufficient power density to ionize the air. The waist of the laser is positioned such that the plasma spark is approximately in the center of the spark gap, a configuration that has been shown to provide the most efficient

switch-triggering characteristics [14]. The alignment of the plasma spark is performed by visual inspection and results in an error of ± 0.5 mm.

At the triggering laser conditions used, the laser induced plasma spark is sufficient to induce switch closure for self-break percentages as low as 40%. To achieve this, the laser energy is higher than the 0.5 – 5 mJ energies used in fiber delivered versions of this switch [14]. The high laser energy was preferred in this work as it allows to repeatable plasma formation (100 % switch closure at conditions of interest) while allowing slight variations in alignment between the triggering laser and the focusing optics. The ability to have minor changes in alignment while maintaining performance was essential for the work in this thesis due to the non-idea laboratory conditions (optics were not vibrationally dampened and existed on different tables/surfaces). The downside of using a higher than required laser energy is that a significant portion of the incident laser energy is not deposited into the plasma but instead impinges on the capacitor-side electrode, resulting in minor sputtering.

The conditions for the switch operation were carefully curated to allow for Laser Thomson scatter on the plasma channel. This further signals a departure from typical HV-LTS switch operation but does not change the fundamental physics being investigated in this thesis (change in plasma conductivity during switch closure). A major concern for Thomson scattering is the viable range of electron temperatures and densities that are measurable for a laser-induced plasma (LIP). The restrictions of Thomson Scattering prohibit measurements of plasma properties in LIP for delay times earlier than 80 ns [24,64]. To perform laser Thomson scattering within the switch, the switch run-time (time between LIP formation and switch closure) to be greater than 100 ns (verses the typical values of less than 10 ns for a HV-LTS in a pulsed power application). The selected

run-time for this work is 120 ns as this provided a sufficient delay with minimal jitter in switch closure (7 ns based on extrema of repeat measurements).

2.4 Aqueous Variable Impedance Load

As mentioned, the previous HV-LTS testbed operated with a short circuit and had strong reflection in the current. [14,21]. Although the short circuit configuration provided similar physics during the rising edge of the current pulse, it does not provide an accurate representation of a pulsed power application due to lacking a load. To emulate a proper pulsed power load, an aqueous variable impedance load (AVIL) has been designed [65]. Figure 1-4 depicts the load implementation including the AVIL, a diaphragm pump, valves, and a liquid reservoir.

The geometry of the aqueous load was designed to have similar dimensions as the capacitor it replaced, resulting in a compact circuit that minimizes transmission losses and transmission line charge storage.

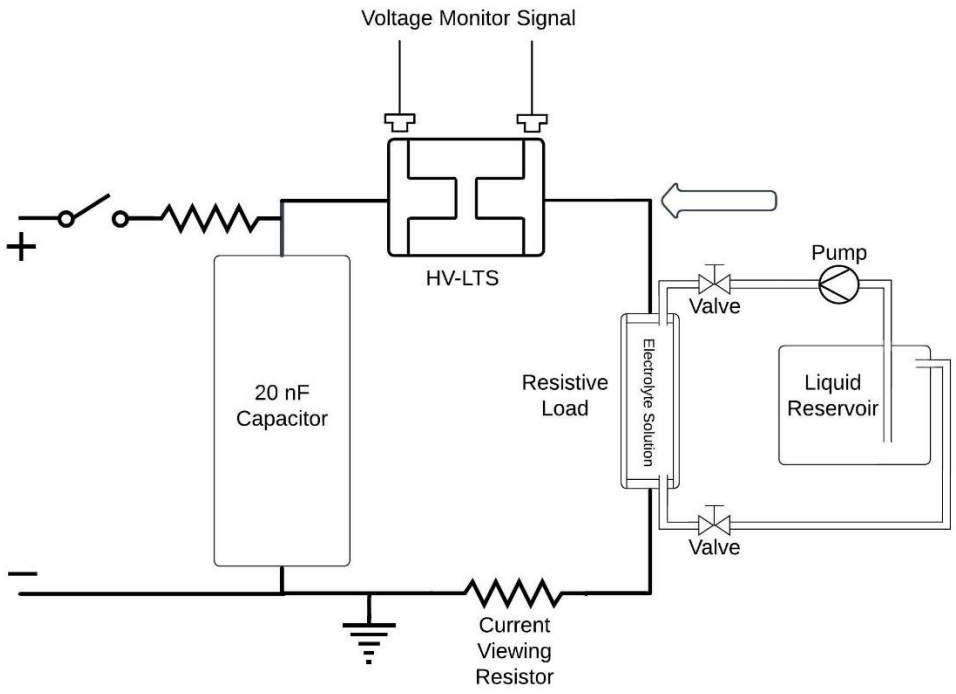

Figure 2-4 Schematic of HV-LTS testbed showing liquid exchange and processing loop.

Figure 1-5A is a representation of the physical electrical circuit and figure 1-5b. is a drawing of the AVIL cross section. The AVIL electrodes are made from cast stainless steel for chemical compatibility with the electrolyte solution. In each electrode, there is a threaded hole where the transmission line brackets are attached as well as a threaded port for liquid exchange. From electrical stimulations of the circuit, it was determined that the load must have sub-ohm tunability in the range of 4 – 8 Ohms. With this resistance range, geometric constraints, and simplicity of operation in mind, the electrolyte solution was chosen as sodium chloride (NaCl, table salt) in distilled water. The result is an AVIL that is tunable between 2 - 100 Ω where the upper bound is determined by the purity of water used (and possible corrosion of the electrodes).

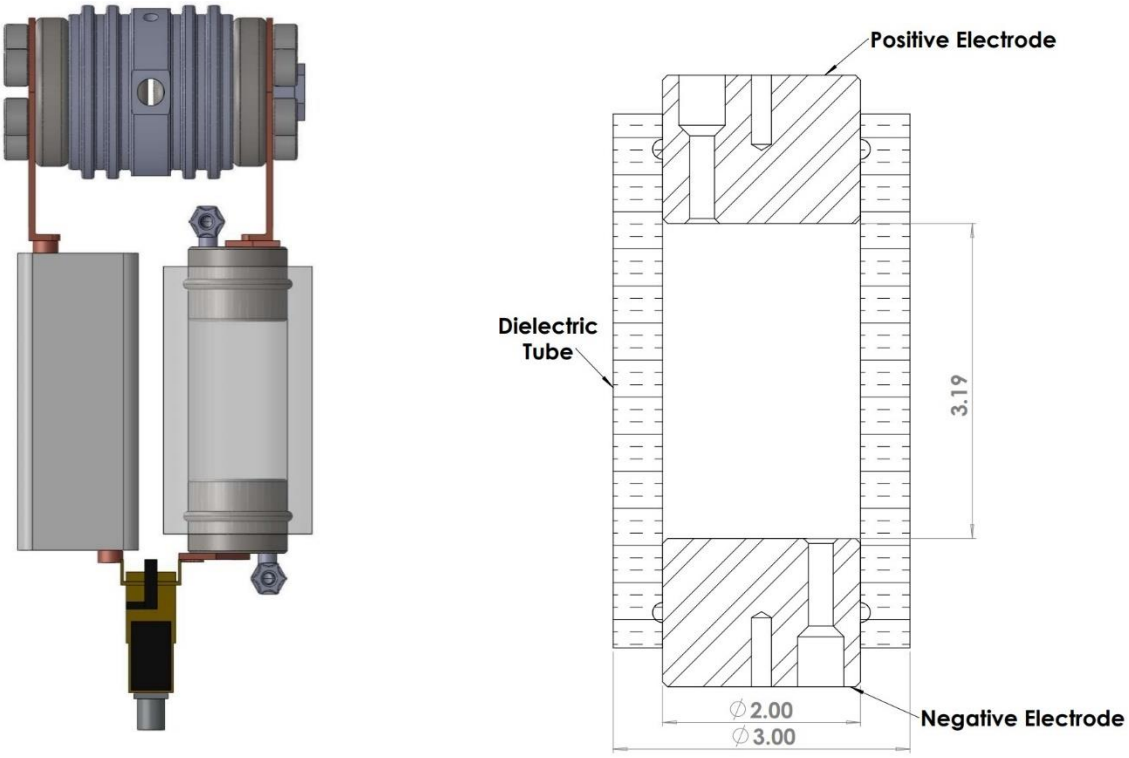

Figure 2-5 A) Physical representation of HV-LTS electrical circuit. B) Cross-section of aqueous variable impedance resistor.

To allow the load impedance to be tuned *in situ* (and without changes in optical alignment), a liquid exchange loop and reservoir were added. The larger volume of water in the reservoir lowers the sensitivity solution concentration by requiring large mass changes in salt which in turn improves the precision of resistance tuning for the load. Another benefit of the liquid exchange loop is that one can match the load impedance to the driving circuit without needing to measure the exact resistance of the circuit (a challenging task for pulsed power systems).

During data collection, the valves on the liquid exchange loop are closed to maintain an approximately constant load impedance. Due to separation of the electrolyte solution and corrosion of the electrodes, there is a change in load impedance over time, however, there is not a noticeable

change in switch current traces over measurement time-scales. Figure 2-6 is data of the current traces, as measured by the current viewing resistor (CVR, T&M Research Products W-2-001-6FC), for cases of the original short-circuit current (with two capacitors), matched impedance, overdamped, and underdamped load for a 6 kV charged capacitor. Where time zero is referenced to the time of the triggering laser pulse. Comparing the short-circuit and circuit with a load, there is a clear reduction (to the point of undetectable) in current-reflections. It is also clear that the higher impedance of a load-based circuit slows the rising edge of the current pulse.

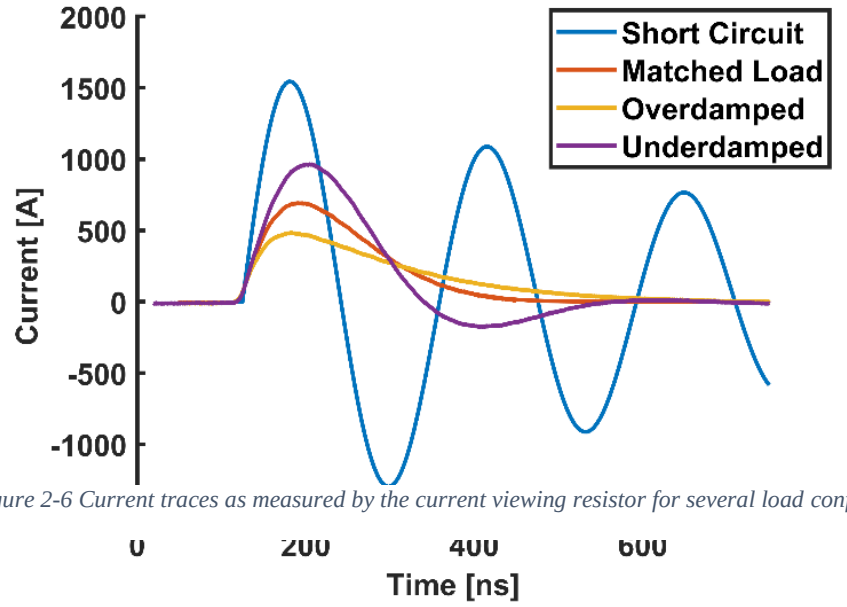

Figure 2-6 Current traces as measured by the current viewing resistor for several load configurations.

Figure 2-7 are the same current traces as Fig. 2-6, normalized to the peak value. From the comparison of normalized current traces, it is seen that the characteristic rise time and general trend of the current pulse rising edge is not affected by the load. During the rising edge of the current pulse, the electrical characteristics are dominated by the pulse forming network.

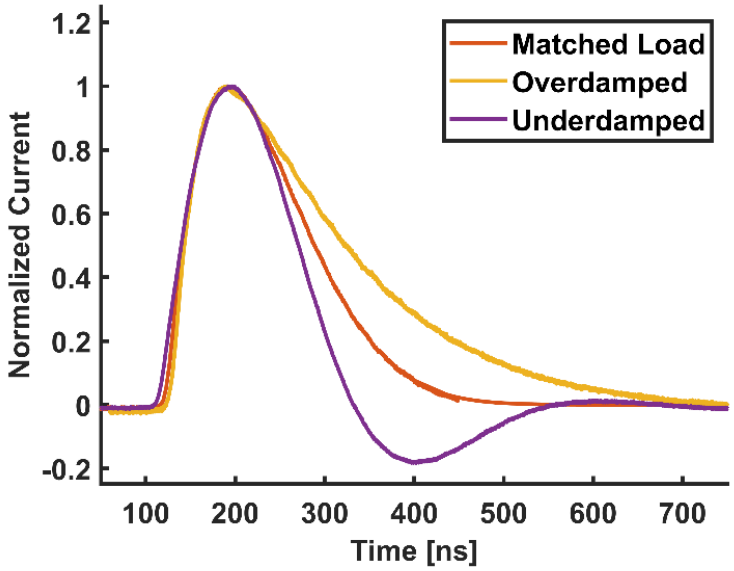

Figure 2-7 Normalized current traces from figure 2-6

CHAPTER 3: OPTICAL AND ELECTRICAL DIAGNOSTICS

3.1 Laser Thomson Scattering

3.1.1 Experimental Optical Layout

Figure 3-1 is the experimental optical layout for the Thomson Scattering measurements in this work. The probe laser is a frequency doubled Nd:YAG (Quantel Q-Smart 100) operating at 532 nm with a pulse energy of 28 mJ and duration 8 ns (FWHM). A variable attenuator, consisting of a half-waveplate and polarizer, is used to define the final beam energy and set a linear polarization which is perpendicular to the plane of the scattering. Thomson Scattering is sensitive to laser polarization and therefore, the half-waveplate ensures only laser energy with a polarization contributing to Thomson Scattering reaches the plasma. The removal of additional polarization components limits unnecessary heating of the plasma through inverse-Bremsstrahlung absorption.

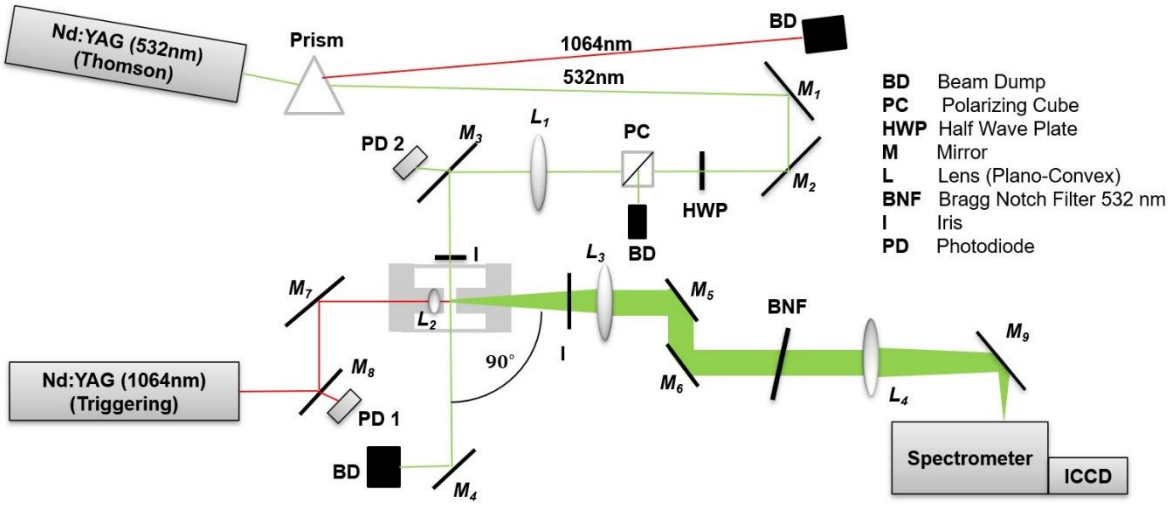

Figure 3-1 Optical layout for laser Thomson scattering [44]

Figure 3-2 are experimental data from an investigation of laser pulse energy and electron temperature and density measurements. From the data, it was determined that 28 mJ was the maximum laser energy one could use before noticeable perturbation is detectable.

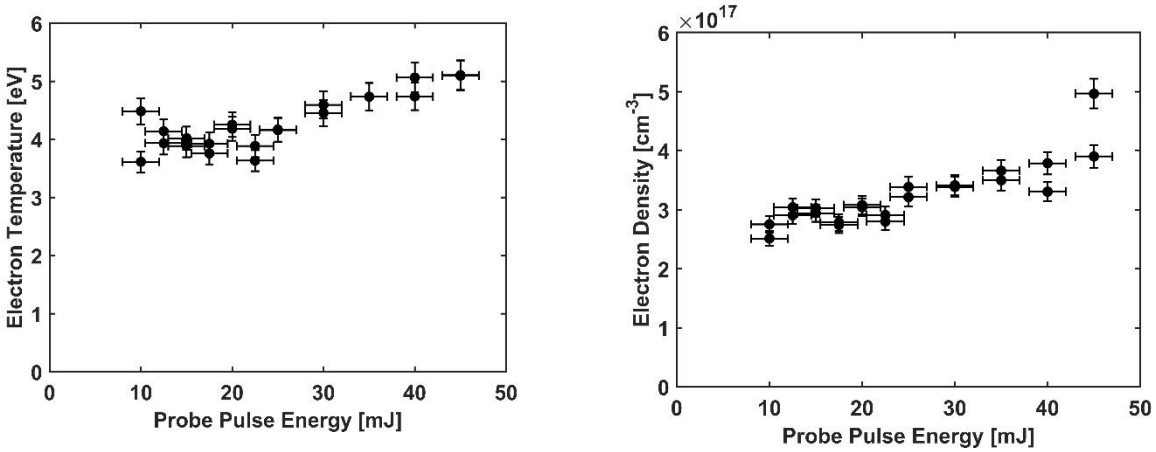

Figure 3-2 Comparison of probe laser pulse energy verses measured plasma electron Left) temperature and Right) number density.

To further reduce the effects of heating the plasma with the probe laser, the probe laser is weakly focused by a lens (L_1, f = 400 mm) such that the waist is located at an iris upstream of the switch. The beam expands to a diameter of approximately 0.9 mm in the region of interaction with the plasma channel, resulting in a laser fluence of approximately 1.1 J/cm^2. The laser fluence is several orders of magnitudes below what is commonly used in laser Thomson scattering [24,55,66–70]. In addition to limiting heating of the plasma, the diameter large diameter of the probe laser is larger than the diameter of the plasma channel at early times, ensuring the entire plasma channel diameter is probed with an approximately constant fluence. By ensuring the beam is larger than the plasma also allows for slight spatial variations in the plasma channel and optical components.

In typical laser Thomson scattering optical systems, the plasma being probed is within a chamber that has extended arms consisting of Brewster angle windows and a series of baffles [71]. The aim of these components is to minimize elastics (laser line) scattering which tends to saturate detectors and obscure the Thomson scattering signal. These concerns are elevated for applications within high voltage switches as the plasma is located between two reflective electrodes. For this work, a simplified version of a baffle system is implemented and consists of a single iris (I_1) located at the probe beam waist. The iris removes the divergent components of laser light, resulting in minimal elastic scattering from switch surfaces as seen in figure 3.3.

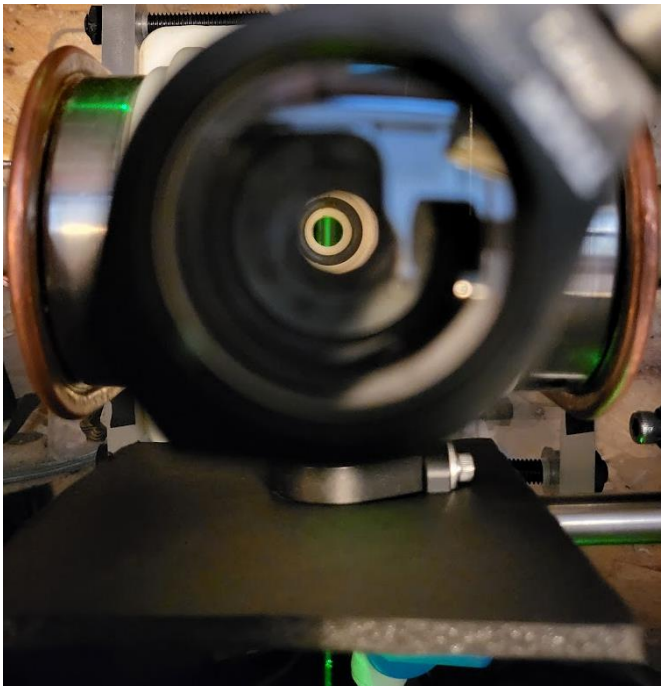

Figure 3-3 Picture of Thomson Probe laser within switch. Both switch electrodes are visible without any noticeable elastic scattering.

The scattered light, along with the plasma luminous emission, is collected and collimated by a 150 mm focal length plano-convex lens at 90 degrees (L_3). The collection volume of the lens is limited by an iris (I_2) to both restrict the overall luminosity and improve collimation (for optical

Bragg Filter performance). To avoid saturating the detection equipment or distorting the Thomson scattering signal, the Rayleigh and elastically scattered light is filtered with a Bragg Notch filter. The Bragg Notch filter attenuates collimated 532 nm (FWHM 0.1 nm) light by an optical density of approximately 3-4. After the Bragg Notch Filter, the collected light is one-to-one imaged onto the 40 μm slit of a spectrometer (Princeton Instruments SP-2300i) where it is dispersed with a 1200 groove/mm grating onto the ICCD (Princeton Instruments PI-MAX4) using a gate width of 10 ns. This results in a spectral resolution and wavelength range of 0.030 and 30 nm respectively. The collection optics are aligned such that the preserved spatial dimension is along the probe laser and imaged along the spectrometer slit. The scattering volume (as seen by the ICCD sensor) from this optical layout is 8 mm along the probe laser axis, 40 μm in the probe laser radial direction (plasma axial direction), and 0.9 mm into the page as presented in figure 3.3. The preserved spatial resolution allows one to record spatially resolved Thomson measurements of the plasma channel [21], however, the ICCD output is averaged over all spatial dimensions to improve the collected Thomson scattering signal. In turn, all Thomson measurements reported in this work are averaged over the plasma channel radius.

3.1.2 Timing

Due to the fast temporal evolution of current and the transient nature of the plasma channel in HV-LTS's, precise timing control of diagnostics is essential. Control of the experimental set up consists of two timing regimes, a slow charging phase (order seconds) and a fast diagnostic phase (order nanoseconds) which are controlled by separate systems. The nominal timing of the overall system is controlled by an Arduino powered Maser Control box (MCB) (MCB) [3]. The MCB controls the switch gas purge and charge control. Once the capacitor is charged to the desired

voltage, the MCB activates the isolation relays and sends a signal to a delay generator (Sandford Research Instruments DG535). The delay generator has sub-picosecond jitter and allows for accurate timing of switch triggering, the Thomson probe beam, and the ICCD gate time.

During the diagnostic phase, the reference time (t_0) is considered as a 10% rise in signal from photodiode 1 in figure 3-1 (the time of the triggering laser). The reported value for the delay between the plasma forming laser pulse and the diagnostic laser pulse is determined by the signal from photodiode 1, photodiode 2, and the monitor signal on the ICCD as displayed on an oscilloscope (RIGOL S1204B).

To minimize effects of cable delays, all signals are transmitted by triple-shielded coaxial cables that have been measured to have a one-way transmission time of 18 ± 2 ns. The jitter of the triggering and probe laser are 4 and 3 ns respectively. The jitter of the ICCD gate is considered negligible. From an analysis of standard deviation in overall system jitter, the timing accuracy of Thomson scattering diagnostic is ± 6 ns. However, this is further increased by post-processing and switch closure jitter to ± 10 ns.

3.1.3 Data Collection

Due to the small scattering cross section of Thomson scattering, the scattering power is weaker than the plasma luminous emission for many conditions of the electrically excited plasma. For example, during the main current pulse, emission lines from the plasma can be 100 times greater than the Thomson scattering peaks which is seen in figure 3-4. To improve the signal to noise, and allow the detection of the Thomson features, several steps were taken. The first was the use of shot averaging. For each temporal datapoint, spectra of 200 individual switch firing events were recorded and averaged for both the plasma with the Thomson Probe laser and of the plasma

emission alone. These two spectra are then subtracted, isolating the Thomson scattering (and other effects of probe laser perturbation).

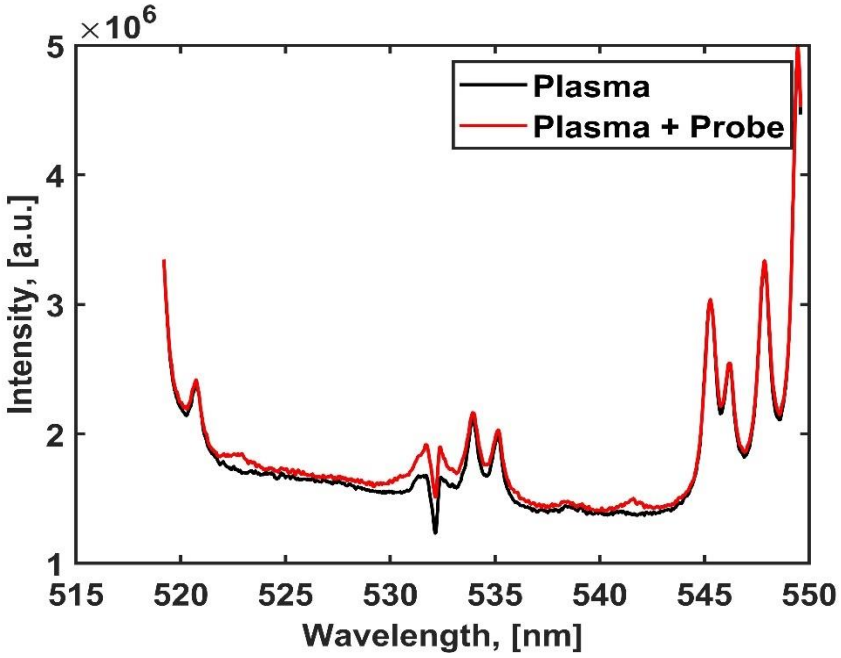

Figure 3-4 Plasma spectral emission with and without the probe laser. Thomson scattering features are visible at 521 and 543 nm while elastic scattering features are located near 532 nm.

To further improve the quality of isolating the Thomson features, the recorded spectra were time binned (with respect to a reference current temporal profile) based on the luminosity of plasma emission at 525 nm. There is no emission line at this wavelength and therefore only electron continuous emission is measured. This binning method is essential in eliminating the effects of jitter in switch closure time. The switch closure has a jitter of 7 ns (as determined by extrema of repeat measurements) which results in considerably different plasma conditions during the 45 ns rising edge of the current pulse, when conditions are measured at a constant time delay from the triggering laser. Changes in background plasma conditions from shot-to-shot will overshadow the Thomson features making their detection impossible. This concern becomes

increasingly important as the Thomson features can overlap with emission lines and plasma emission line intensities are directly related to the plasma electron temperature and density [72,73]. From an investigation of the plasma luminosity verses the temporal evolution of the current pulse, figure 3-5, it was determined that the plasma luminosity can be used as a stand in for time rather than the specified delay time, allowing for consistent plasma background subtraction.

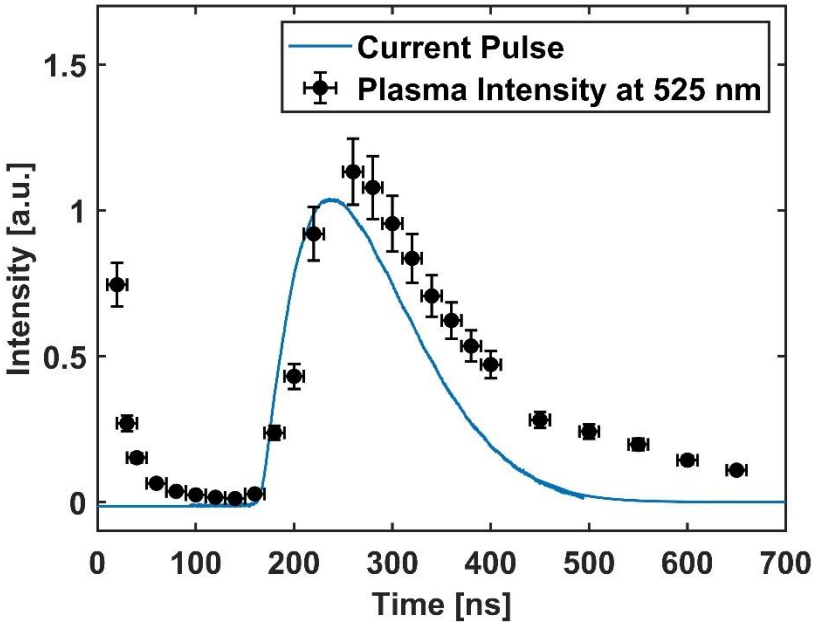

Figure 3-5 Plasma luminous intensity compared to the temporal evolution in current flow. Note that between t0 and 180 ns, the laser induced plasma alone is present.

3.1.4 Data Analysis

To determine the plasma electron density and temperature from the experimental Thomson spectra (which is the result after subtracting the plasma background) a fit of a synthetic Thomson spectrum is used. To produce the synthetic Thomson spectra, the Thomson scattering form factor in equation 1.5.8 is used. To improve the accuracy of the synthetic spectrum, a calibration is performed by rotational Raman scattering by calculating a scaling factor, M :

$$P_i \Delta\Omega \ell \epsilon = \mathrm{M} = \frac{P_{J\to J'}}{n_J \cdot \frac{64\pi^4}{45\varepsilon_0^2} \cdot b_{J\to J'} \cdot \frac{\gamma^2}{\lambda^4_{J\to J'}}} \tag{3.1.1}$$

where ℓ is the *collection extent*, ϵ is the *collection efficiency* [47]. This scaling factor is determined by an automated fitting code that performs a least-square difference between a rotational Raman scattering spectrum and a simulated rotational Raman scattering spectrum. This calibration method also allows for an accurate wavelength calibration which allows for accurate detection of plasma emission line.

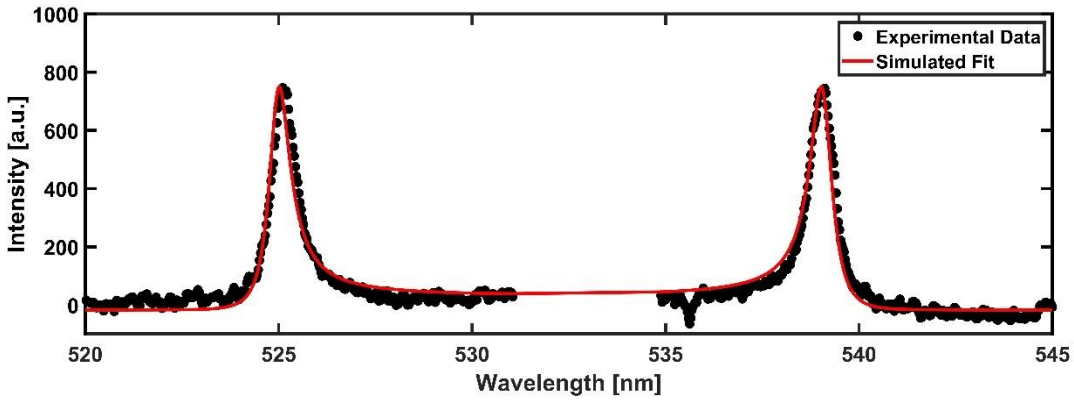

Figure 3-6 Synthetic Thomson scattering spectrum fit to experimental data.

After the calibration with rotational Raman scattering the simulation has two free variables, the electron temperature and density. These two variables are then systematically checked until the best synthetic spectrum is found for the experimental spectra. The best fit is determined by a minimization cost function of difference of squares. Figure 3-6 is an example of a fit corresponding to an electron temperature of 3.5 eV and electron density $3.5\text{x}10^{17}$ cm^{-3} to an experimental spectrum taken at a delay time of 450 ns for a 6 kV excited plasma.

To verify the simulation and fitting method, a comparison is made with published data by Dzierze ega et. al. in which they investigated the temporal evolution of a laser induced plasma in

atmospheric condition air [24,64]. Their work measured a plasma spark induced by a 4.5 ns FWHM, 532 nm Nd:Yag with a fluence of 5.5 kJ/cm^2. This varied from the verification experiment which used a 14 ns FWHM, 1064 nm Nd:Yag with a fluence of ~ 20 kJ/cm^2. Although the conditions are slightly different, similar plasma conditions are produced, allowing for calibration within our error margin. Figure 3-7 is a comparison between the plot from Dzierze ega et. al. (left) and the results of the verification experiment (right).

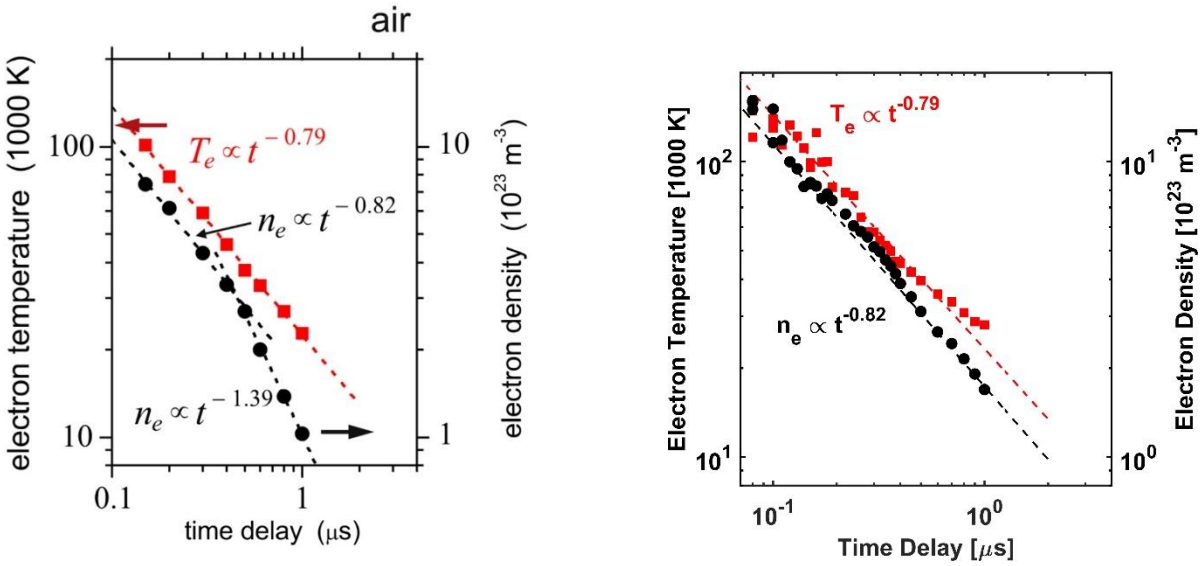

Figure 3-7 Left) Temporal evolution of laser induced air plasma measured by Dzierze et.al. [24]. Right) Experimental data of laser induced plasma in air. Similar trends and magnitudes are observed.

From the comparison, it is found that the data using the experiment setup and data analysis in this work matches the published values in both magnitude and trend. It is therefore considered that the data analysis method is valid.

3.2 Electrical Diagnostics

To investigate the plasma conductivity in a wholistic approach and verify if the assumptions in the Martin/Braginskii Model are accurate, this work aims to measure the transvers switch conductivity through electrical measurements. To determine the plasma channel conductivity, accurate measurements of the voltage drop across the plasma channel and current passing through the plasma channel are required. Direct measurements of these quantities are exceedingly challenging and therefore the measurements used are lump sum characteristics for the switch. For the voltage drop, we are considering the voltage difference between electrodes, combining the resistance of plasma surface interactions and the plasma resistance. For the current, the overall circuit current is measured.

3.2.1 V-Dot Probes

For electrode voltage measurements, this work used V-Dot probes. V-Dot probes are capacitive voltage monitors that respond to changes in the electric field and therefore produce a derivative response. When compared to resistive voltage monitors, V-Dot probes have three major advantages. The first major benefit is that V-Dot probes are a non-contact and non-perturbative method of voltage measurement. This is essential an essential requirement for pulsed power applications as resistive voltage monitors provide a path to ground. Although resistive monitors typically have several megaohm resistances, this is lower than the open spark gap resistance before laser triggering. The result of this path to ground is a current drawn from the charge capacitor during the isolation phase, unpredictably changing the switch voltage during operation. The second major benefit of V-Dot probes is their high bandwidth to cost ratio, with the ability to buy probes with picosecond response times for a fraction the cost of a resistive monitor. Additionally, unlike resistive monitors, the bandwidth is not determined by onboard circuitry but instead by the

equipment used to process their signal. Further, there is no significant current passing through a V-dot probe, so, there is no concern of heating its internal components and in turn V-dot probes do not have a measurement time limit. Finally, V-Dot probes don't suffer from a resistive voltage coefficient allowing for measurement of up to megavolt potentials where resistive monitors are infeasible.

Due to the derivative-coupled nature of V-Dot probes, one needs to integrate the signal to determine the change in voltage [11]. There are two main methods of integrating the V-Dot probe signal, direct numerical integration and analog integrating circuits. Direct numerical integration is the simpler route, however, due to the derivative response, signals often have high frequency information that may be aliased by low cutoff frequency oscilloscopes. Should aliasing occur, error in numerical integration will result in erroneous data. As there is no way to know if aliasing occurred without knowing the original signal, the only solution is to use a high sample rate oscilloscope which quickly becomes cost prohibitive. Alternatively, one can use an analog resistor-capacitor (RC) integrator (depicted in figure 3-8), lowering the oscilloscope sample rate requirements with minimal loss of high frequency information, assuming a high-performance and properly selected RC integrator was used. For this work, an analog RC integrator is used due to the lower equipment requirements. Although analog integration requires

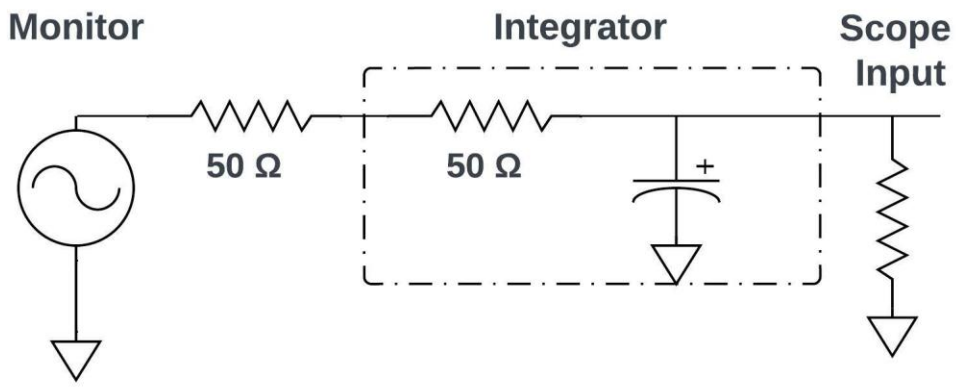

Figure 3-8 Analog RC integrator circuit

less expensive recording equipment, the capacitive nature of the RC integrator results in an inability to transmit DC voltages. Another drawback of RC integrators is that the nature of the RC integrator also results in an associated voltage droop in the output signal. Equation 3.2.1 is used to correct for integrator voltage droop based on empirically measured RC time constant, τ [74].

$$S(t)_{corrected} = S(t) + \frac{3}{2\tau}\int_{t_{start}}^{t} S(t')\,dt' \qquad (3.2.1)$$

where S(t) is the *measured output voltage* and τ is the *RC time constant*. To ensure proper integration, one wants to select an RC integrator with a time constant larger than the signal being measured. The integrators used for this work have a time constant of ~ 1 μs, five times longer than the measured voltage signal. Figure 3-9 is an example of the droop correction performed on the integrated V-Dot signal for the negative electrode during switch closure.

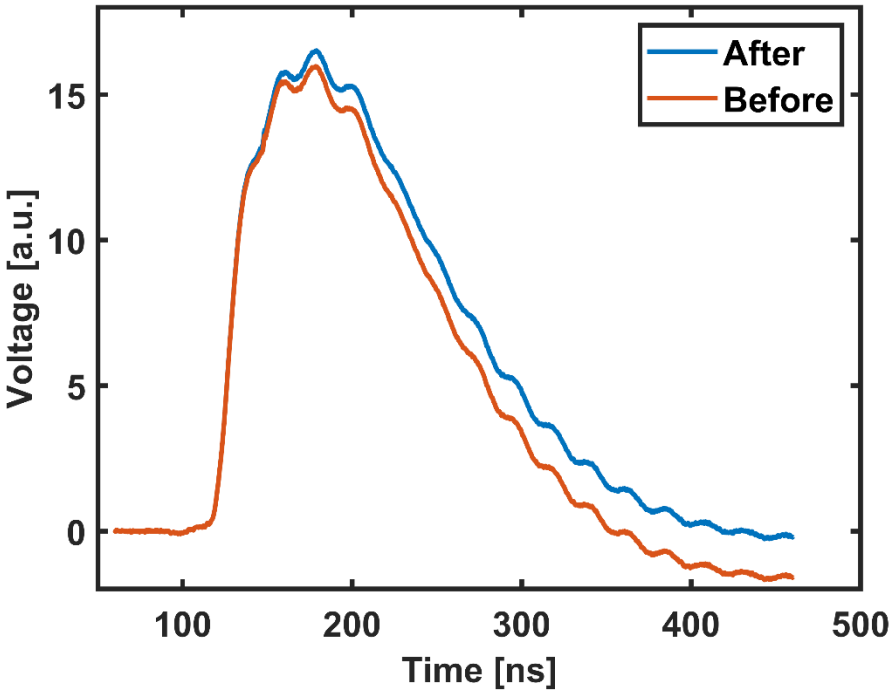

Figure 3-9 Negative electrode V-Dot probe signal before and after droop correction.

One downside to using V-Dot probes is that since they respond to the electric field, their output signal must be calibrated to their location within the electric field. For this work, the calibration was performed by measuring 200 signal traces with a calibrated resistive voltage monitor (Tektronix P6015A) attached to an electrode and 200 signal traces (due to the same switch closure events) with a V-Dot probe using an analog integrator on an oscilloscope (Tektronix TDS5034B). For improved accuracy, the 200 traces are averaged. The droop corrected V-Dot signal is fit to the resistive voltage monitor signal with a linear transformation and the best fit is determined by a cost function minimization of the residual sum of squares for the two signals. The error in fit coefficients was determined using the root mean square of the resistive voltage monitor error, oscilloscope error, and statistical variance of the 200 shot averages.

3.2.2 Current Viewing Resistor

For current measurements, this work uses a current viewing resistor. A current viewing resistor (CVR) is a high-power low resistance resistor that is calibrated with high precision and accuracy. The model used in this work is the T&M Research Products W-2-001-6FC with a resistance of 0.0098 Ω and a pulse energy rating of 275 J. The resistor is added in series with the switch and is the component separating the switch from ground. In this configuration, the current viewing resistor sees all current that flows through the switch, and therefore, provides an accurate value of current through the plasma channel.

The output signal of the CRV is the voltage drop across the resistor. The current is calculated through Ohms law based on the known resistance value. Due to the low resistance of the CVR, this calculation is strongly influenced by small changes in resistance. To verify the accuracy of the CVR, the Coulomb transfer is calculated based on the integration of calculated circuit current and compared with the stored charge in the capacitor. The Coulomb transfer from the current calculation is 120 μC which falls directly in the range of capacitor charge, based on capacitor and voltage errors of 10 and 5% respectively, 103 – 139 μC.

CHAPTER 4: RESULTS AND DISCUSION

4.1 Optical Diagnostic Results

The Martin/Braginskii model assumes that a HV-LTS resistance and electrical conductivity are dominated by the conductivity of the plasma channel. The model further states that the plasmas resistivity is calculated through the Spitzer Resistivity (which is a function of the plasma electron temperature as seen in equation 1.3.4) [42] and that the overall plasma channel resistance is determined by radial growth in the plasma channel [3]. This section presents the results from laser Thomson scattering which determine the plasma channel electron temperature used in the resistivity calculation and the electron density which aids in the interpretation of the results. Additionally, optical diagnostics were used to image the plasma channel and characterize the radial growth. The optical diagnostics were applied to two HV-LTS conditions. The two conditions are a capacitor charged to 5 or 6 kV while the load impedance remains constant. This generates a condition with a near matched load (6 kV) and one that is under damped (5 kV) as seen in figure 4-1.

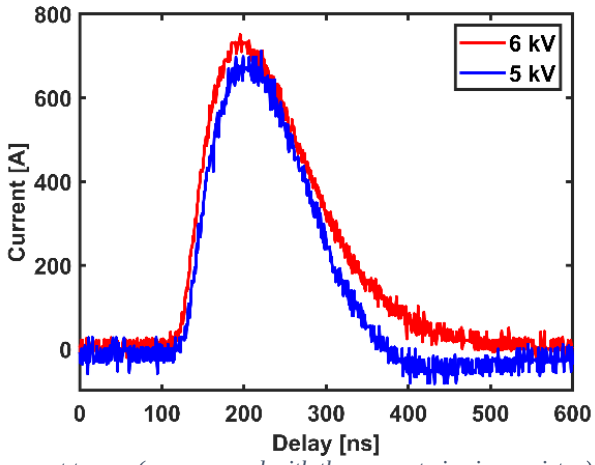

Figure 4-1 Comparison of current traces (as measured with the current viewing resistor) for the two HV-LTS conditions measured with optical diagnostics.

4.1.1 Plasma Channel Electron Temperature

Figure 4-2 shows the measured electron temperature, plotted versus delay (relative to laser trigger), for both the cases of the capacitor charged to 5 and 6 kV. The profile can be considered in three temporal regimes based on switch current flow: A) before current-flow (delay ≲120 ns), B) increasing current flow (delay ~120–220 ns), C) decaying current flow (delay ≳ 200 ns) [44].

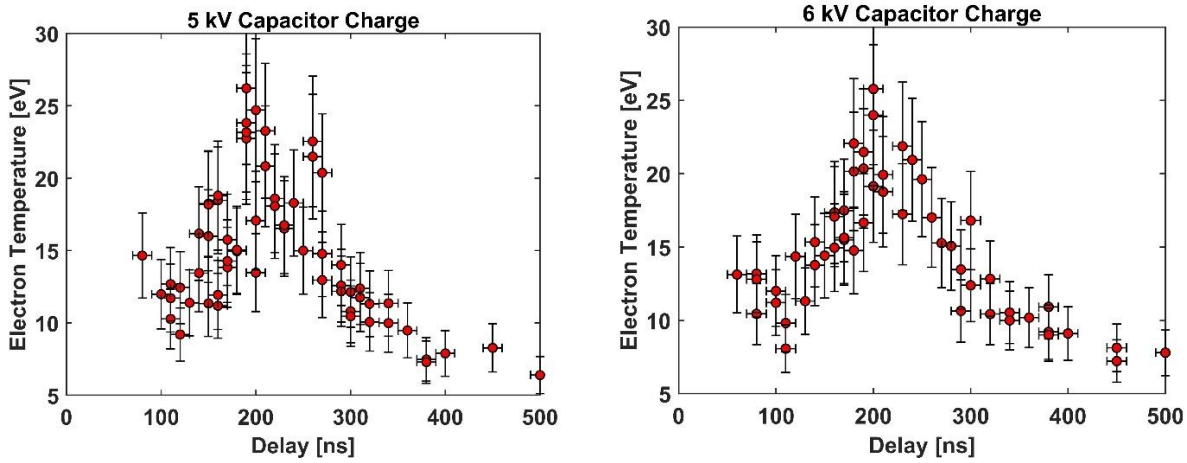

Figure 4-2 Electron temperature evolution for plasma channel in HV-LTS operating with a load voltage of LEFT) 5 kV and RIGHT) 6 kV.

In the first phase, before ~120 ns, the switch has not closed and only the plasma produced by the trigger laser is present. Similar to the plasma luminosity trend in figure 3.5, this laser induced plasma has an initial peak temperature and density (defined by the energy deposition of the trigger laser) which then decay, as would occur in the absence of the switch, until the time of switch closure (current flow) [44]. At 120 ns, the laser induced plasma has decayed to an electron temperature of 9.2 ± 1.8 eV for the 5 kV case and 8.6 ± 1.7 eV for the 6 kV case. These values are comparable to those found for similar laser induced plasma reported in figure 3-7 for a delay time of 120 ns.

The second region commences at the time of switch closure, i.e., onset of current flow, at ~120 ns, and continues until the current maximizes at ~200 ns for the 6 kV case and ~220 ns for the 5 kV case as seen in figure 4-1. Importantly, and in contrast to the assumptions of Martin and Braginskii, Thomson measurements reveal an increasing electron temperature during this phase [44]. For both capacitor charge cases, the plasma electron temperature rises to a maximum value of ~26±5 eV is reached at delay 190 ns for the 5 kV case and 200 ns for the 6 kV case. The maximum temperature occurs near the maximum current flow for the 6 kV case but occurs earlier for the 5 kV case, this discrepancy is likely due to measurement error shrouding the true peak. It is believed that the rise in temperature during the current flow is due to Joule heating [44]. This data represents the first empirically shown breakdown of an assumption within the Martin/Braginski model.

The final temporal section is after 220 ns and corresponds to the falling edge of the current pulse. During the falling edge, we find that the electron temperature decays at a rate proportional to $t^{-1.48}$. A similar rate of decay continues for ~1.5 microseconds following the end of the current pulse. For both the 5 and 6 kV charge cases, the decay in electron temperature matches in both trend and magnitude. This matches the predicted behavior of shock front detachment and cooling of the plasma following the peak of current flow.

4.1.2 Plasma Channel Electron Density

Figure 4-3 is the electron density evolution for the 5 and 6 kV charge cases. As with the electron temperature, the initial laser-induced plasma decays to a value of $1.2 \pm 0.2 \times 10^{18}$ for the 5 kV charge case and a value of $0.9 \pm 0.2 \times 10^{18}$ cm^{-3} for the 6 kV charge case at a delay time of

120 ns. Again, these values are within the error range of the laser induced plasma in figure 3-7, further showing the initial laser induced plasma is not altered by the electric field prior to switch closure. During the rising edge of the current pulse, both cases see a similar rise in electron temperature to a maximum of ~ 2.9 ± 0.6 x 10^{18} cm^{-3} and 3.1 ± 0.6 x 10^{18} cm^{-3} at delay times of 190 and 200 ns for the 5 and 6 kV cases respectively. This matches the delay time of peak values reported in the electron temperature.

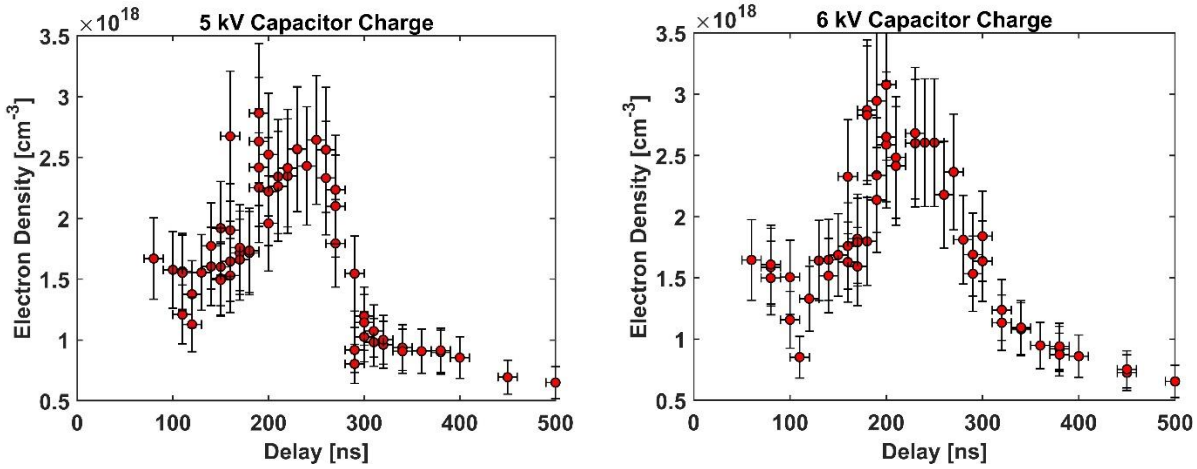

Figure 4-3 Electron density evolution for plasma channel in HV-LTS operating with a load voltage of LEFT) 5 kV and RIGHT) 6 kV.

The maximum electron density represents an ionization fraction of ~0.12 of the ambient air within the switch (assuming singly-charged ions). An important note about the electron density rise during the time of current flow is the current flowing through the plasma channel cannot directly account for it [44]. This conclusion is based on finding that the peak electron density due to the current is ≲10% of the peak electron density measured from Thomson scattering. The former is estimated by temporally-integrating the current signal and dividing it by the approximate plasma volume while the latter comes directly from Thomson measurements (after subtracting the electron contribution from the decay of the trigger pulse). It is believed the rise in electron density

during current flow is due to Joule heating in the plasma (and surrounding gas) leading to an increase in ionization [44].

During the falling edge of the current pulse, the 5 kV charge case with an underdamped load has a sharp decrease in electron temperature until a delay time of 300 ns where it levels off before decreasing again at 400 ns. The reason for this rapid decline and leveling off is not entirely understood, however, this could be an artifact of the current reflection as seen in figure 4-1. The 6 kV charge case, with a matched load, has a slower measured decrease in n_e and does not exhibit a period of leveling off in the decay. At delay times greater than 400 ns, both cases reach similar electron densities and both decay at a rate proportional to $t^{-1.64}$ for 2 μs following the end of current flow. These results qualitatively match simulated results for a laser-triggered plasma channel in air where it was found that, following ionization, there is an initial rapid decline in electron density due to recombination followed by a slower loss of electrons due to attachment [69].

4.1.3 Plasma Channel Radial Growth

To calculate the HV-LTS electrical resistance during operation through equation 1.4.5, the plasma channel radius is needed. Measurements of the plasma channel diameter were completed using the same optical layout as Thomson scattering (without the probe laser) by recording full-chip ICCD images where the spatial dimension (radial dimension of the plasma channel) is preserved. From the ICCD images, the plasma channel diameter is determined by counting the number of pixels (in the radial direction) above a detection threshold and converted to distance using the imaging/magnification ratio and physical ICCD pixel size. To account for the jitter in

switch closure time, the plasma channel diameter is measured ten times for each time step. Figure 4-4 is the experimental data for both the 5 kV and 6 kV charge cases.

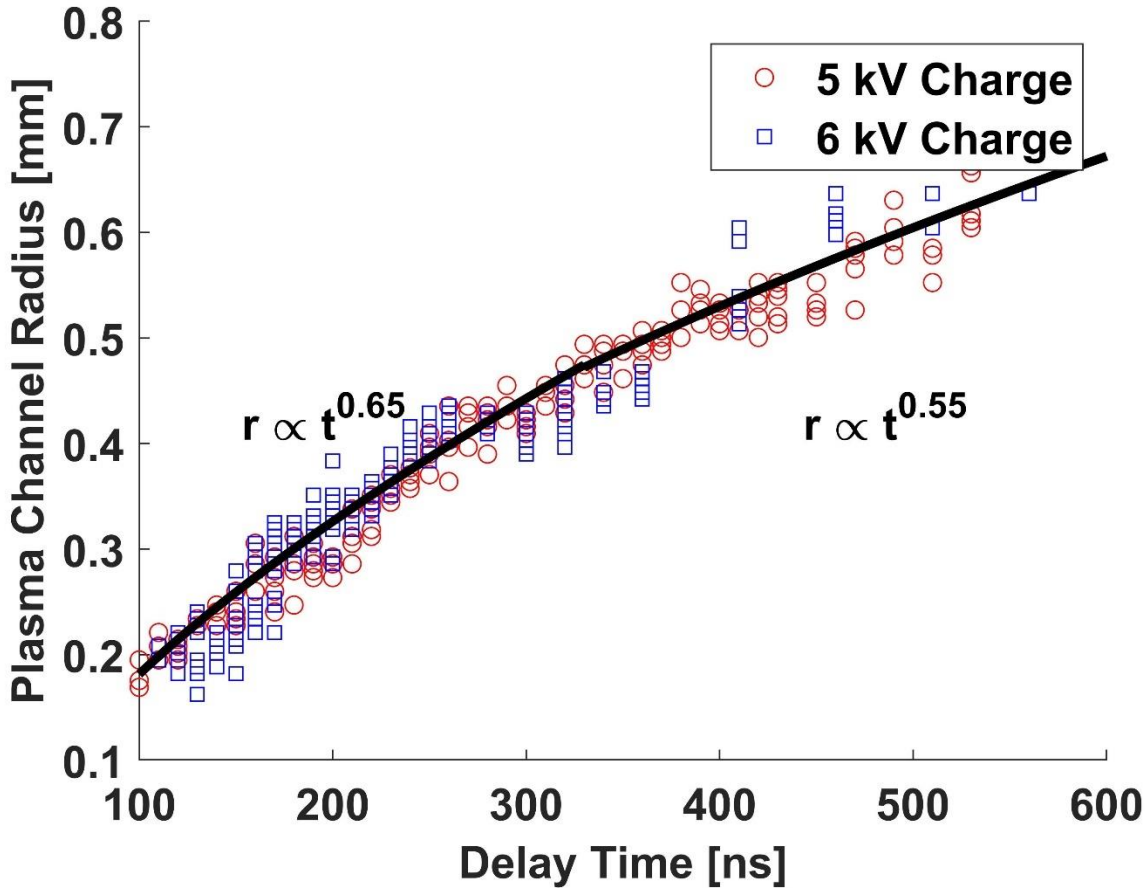

Figure 4-4 Radial Growth of HV-LTS plasma channel for 5 and 6 kV charge cases.

From the data in figure 4-4, it is seen that there are two distinct plasma channel growth rates. There is an initial (faster) growth rate that occurs during the current pulse (120 ns ~ 350 ns) due to the attached shock front and deposited electrical energy. After 350 ns, the rate of radial growth slows due to the detachment of the shock front and end of current transfer but the plasma channel will continue to expand (and cool) for several microseconds [14]. For the 6 kV case, the rate of radial expansion appears to level off between 250 and 320 ns (the falling edge of the current pulse). The

Martin/Braginskii model expects the radial growth (and current transfer) to stabilize at the current flow peak, forming a square wave. Since the same trend is not observed in the experimental current measurements, it is believed that the cause of the constant radius is due to Joule heating equating to energy losses caused by a detached shock front.

For calculations of the plasma channel resistivity, a power law model (which has been verified as an accurate assumption/fit for HV-LTSs) [3,14] is fit to the data in figure 4-4. The resulting fit for the plasma during the current pulse (for use in future calculations) is:

$$r\,[mm] = 0.011t^{0.65} \tag{4.1.1}$$

This matches rate of plasma channel expansion for a variety of high-voltage spark-gap switches operating under a variety of conditions in literature which are tabulated in table 4.1.

Table 4.1 Comparison of Power law Rates

	K	**R^2**
MARTIN FIG. 1 [3]	0.644	0.989
MARTIN FIG.13 [3]	0.575	0.983
WOLFORD [13]	0.580	0.974
ROSE 50 KV [14]	0.661	0.982
ROSE 100 KV [14]	0.727	0.974
GOTTFRIED	0.654	0.973

4.2 Electrical Diagnostic Results

Using the calibrated V-Dot probes, the voltage of both the positive and negative electrodes was recorded during switch operation. For the electrical measurements, the capacitor was charged to a constant value of 6 kV while the load was changed such that several conditions were tested. The conditions investigated include an underdamped (~4 Ω), overdamped (~10 Ω), and matched (~6 Ω) impedance load case. For each case, 200 single switch events were recorded and averaged to reduce noise. Figure 4-5 A-C are the electrode voltages present for each load case.

A)

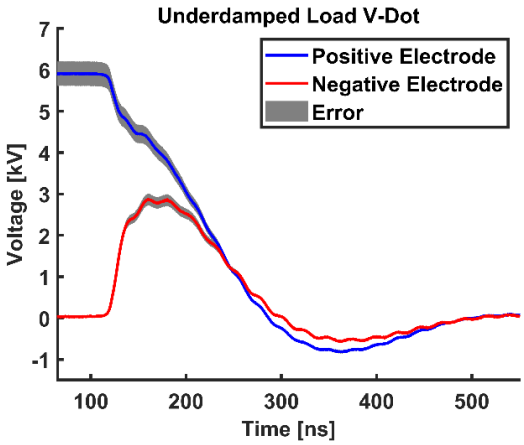

B)

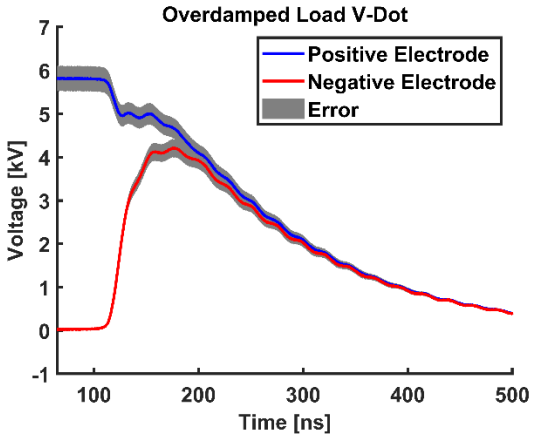

C)

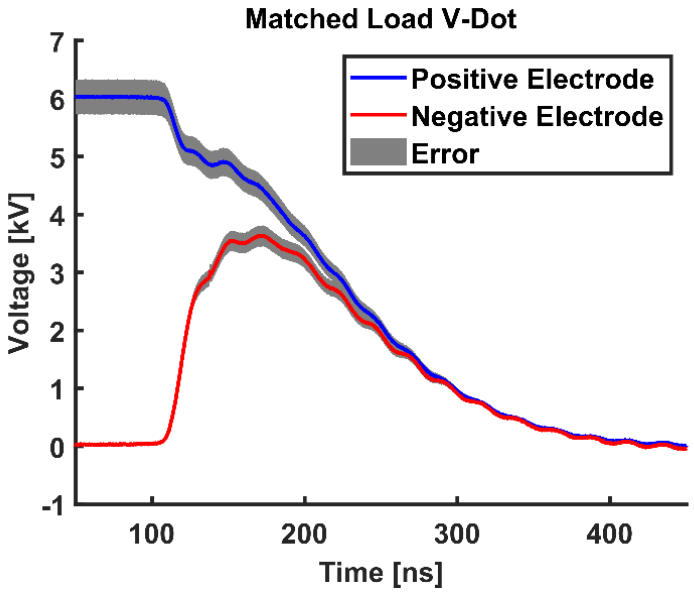

Figure 4-5 Calibrated V-Dot signals for corresponding to a 6 kV capacitor charge with a A) underdamped load, B) an overdamped load, and C) a matched load.

From the voltage signals present in Fig. 4-5, the voltage drop across the plasma channel is calculated. The voltage drop is used in combination with the currents measured with the CRV in Fig. 4-6 to calculate the plasma channel impedance according to Ohm's law:

$$R_{plasma} = \frac{V_{drop}}{I} \tag{4.2.1}$$

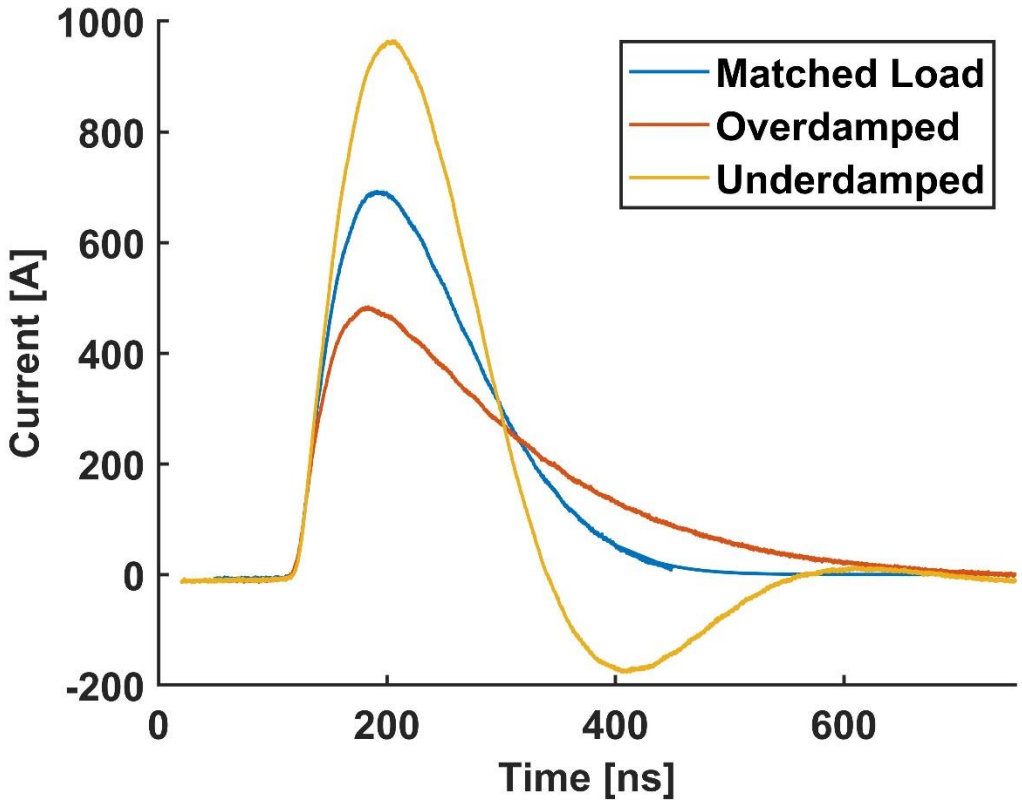

Figure 4-6 Current traces for each load configuration

Figure 4-7 is the impedance of the plasma channel, calculated by equation 4.2.1, plotted against the delay time for the underdamped, overdamped, and matched load case. In all cases, the capacitor was charged to 6 kV resulting in the same pulse forming network configuration for each case. As with the rising edge of the current, it is expected that the impedance collapse during the rising edge will be determined solely by the driving pulse forming network (capacitor in this case). The measured impedance collapse does follow this trend with minimal difference in the impedance collapse for different load cases.

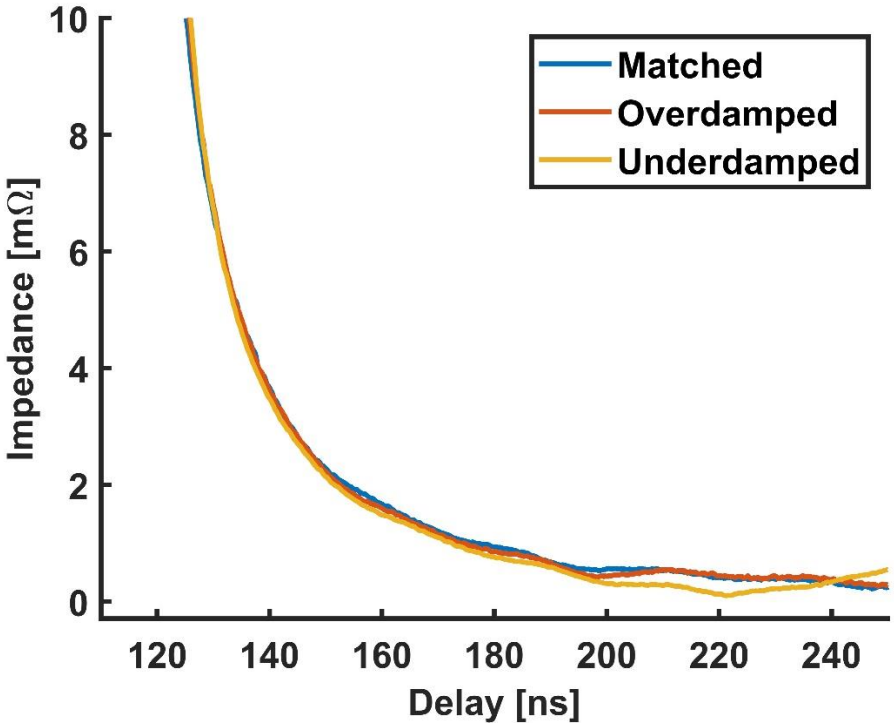

Figure 4-7 Comparison of impedance collapse during the rising edge of the current pulse for three load configurations.

Using the values for impedance calculated with equation 4.2.1 and the plasma channel radius calculated with equation 4.1.1, equation 1.4.5 can be used to calculate the conductivity of the plasma channel which is plotted in figure 4-8. It was found that for the conditions and switch studied, the plasma channel conductivity is linearly increasing during the rising edge of the current pulse [11]. This directly contradicts the assumption used to derive the Martin/Braginskii model (equation 1.4.4) that stated that changes in the electrical conductivity are negligible during the operation of the HV-LTS.

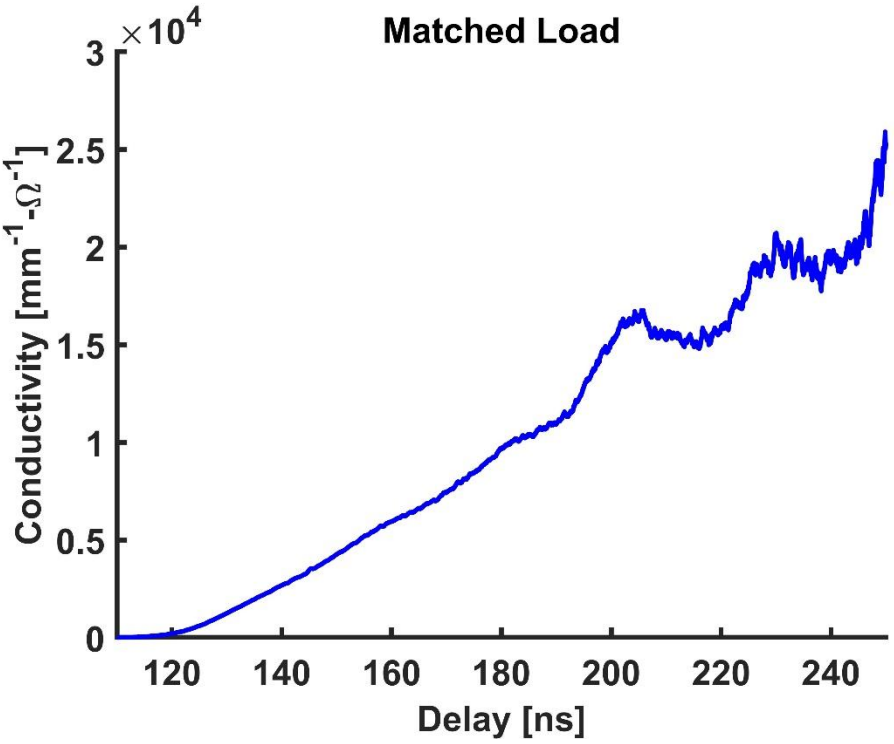

Figure 4-8 Plasma channel conductivity for the matched load case during the rising edge of the current pulse.

4.3 Comparison of Optical and Electrical Diagnostics

As discussed in section 1.4, the Martin/Braginskii model uses the Spitzer resistivity to calculate the plasma channel conductivity [3,36,36,37,42]. Using the plasma electron density and temperature data from Thomson scattering in figures 4-2 and 4-3 for the 6 kV matched load case, the plasma resistivity is calculated using the Spitzer resistivity equation 1.3.4. Continuing, the impedance of the plasma channel is calculated according to [3]:

$$R = \frac{\eta_{Spitzer} L}{\pi r^2} \tag{4.3.1}$$

where L is the *length of the plasma channel* (spark gap distance, in this case) and r is the e*xperimentally determined plasma channel radius* as determined by Eqn. 4.1.1.

Figure 4-9 is the comparison of plasma channel impedance collapse calculated from electrical measurements through Ohm's law and by optical measurements using the Spitzer resistivity model. The Spitzer resistivity model predicts a similar trend for the impedance collapse. However, the predicted resistance is two orders of magnitude greater than the measured impedance.

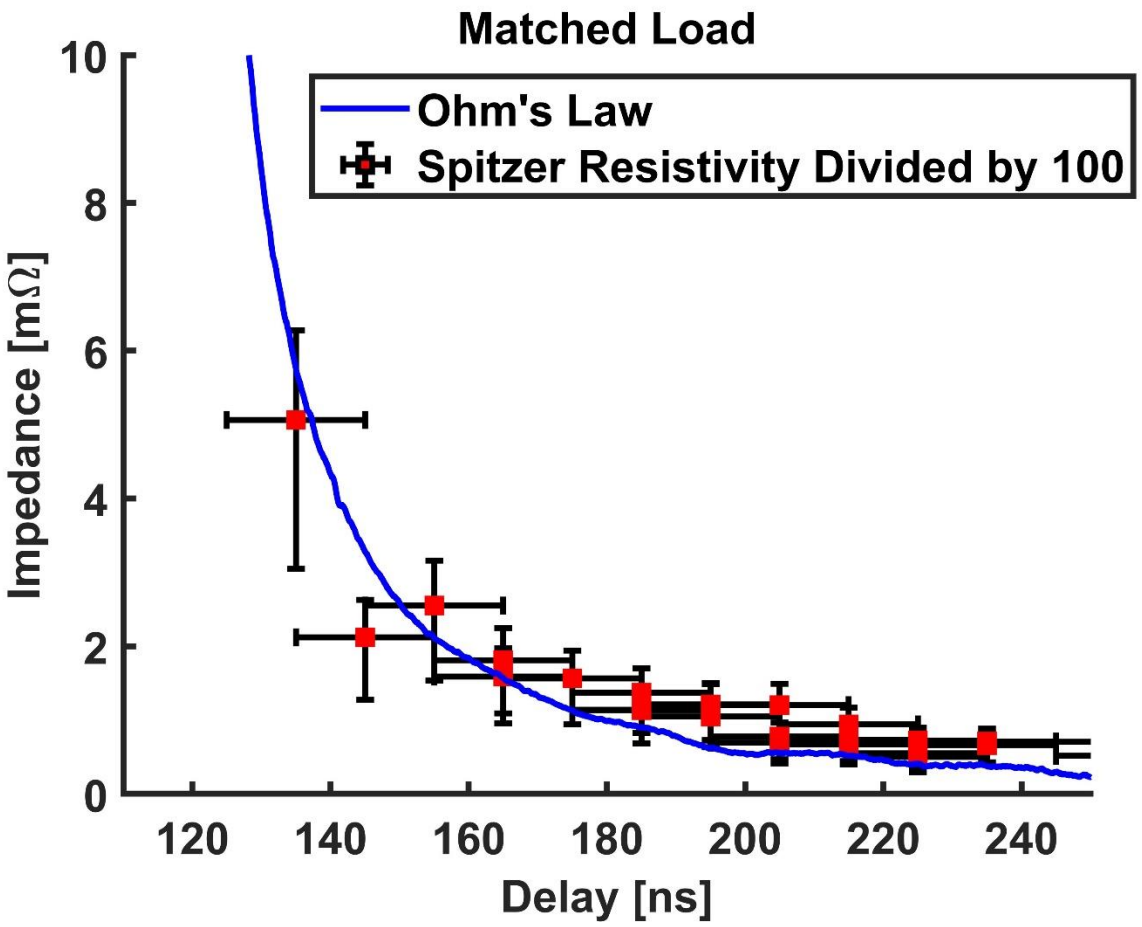

Figure 4-9 Comparison of plasma channel impedance calculated through Ohms law (using electrical measurements) and the Spitzer resistivity (from optical measurements)

This could be the result of incorrect Thomson scattering measurements; however, this is unlikely due to the order of magnitude for the error required to reconcile the difference. The more

likely cause is that the Spitzer resistivity does not correctly model the physics present during the rising edge of the current pulse [44]. For example, the Spitzer resistivity was derived for fully ionized plasma assuming all momentum transfer is from electrons to ions in far range Coulomb collisions [36,39–41]. The plasma investigated in this paper achieves an ionization fraction (assuming a singly ionized plasma and ambient conditions) above 0.1 for less than 100 ns. At a 0.1 ionization fraction, it is likely that the electron-neutral, ion-neutral, and neutral-neutral collisions cannot be ignored as a source of electrical momentum transfer. To achieve an accurate calculation of the plasma resistivity from the plasma parameters, one would use equations (1.3.2) or (1.3.3). This calculation would however require additional information about the plasma chemistry and composition as a function of time as well as detailed knowledge of the bulk gas temperature for the calculation of collisional frequencies. Although it is possible to calculate these quantities, however, the lack of thermal equilibrium, moderate ionization fractions, moderate plasma temperatures, and large gap of unknown plasma properties results in this approach not being tractable in this case.

An additional concern for the comparison of the electrical and optical measurements is that the electrical diagnostic method assumes all electrical losses between the electrodes are resistive losses caused by the plasma (the same assumption made by Martin in the derivation of the Martin model [3]). However, in actuality, there are additional energy loss mechanisms including plasma radiative losses (both heat and light) [76] as well as possible antenna effects generated at the plasma frequency [77]. However, larger voltage drop due to additional loss mechanisms would lead to an overestimate of resistance from Ohms law, leading to a larger discrepancy between the electrical conductivity calculation and the Spitzer resistivity calculation.

CHAPTER 5: CONCLUSION AND FUTRE WORK

The drive to minimize insertion loss mechanisms within HV-LTSs has led to new designs of switches that aim to operate at high currents in the (tens to hundreds of) nanosecond regime. Switches that operate in this regime are characterized by low inductance with short spark gap distances. The design results in HV-LTSs that are dominated by the transient turn on (rising edge of current) and turn off (falling edge of current) times rather than stable periods of current flow. In application, it was found that these new switch designs have behavior that deviated from the simulation codes currently in use. Mainly the Martin/Braginskii model is underpredicting rise times and overpredicting switch on times. The suspected reason for deviations from the modeled behavior are the assumptions used during the derivation of the Martin/Braginskii model. Most notably the assumption of a temporally constant plasma conductivity.

This work aimed to investigate the electrical conductivity through calculations of the Spitzer resistivity model based on data from laser Thomson scattering as well as through Ohms law based on measurements of voltage drop between the switch electrodes. Additionally, the assumption of a power law plasma channel radial growth was verified and a model of radial growth for the HV-LTS under relevant conditions was recorded. From the optical measurements, it was found that both the electron temperature and density vary throughout the current pulse with no sign of stabilization. In turn, calculations of the Spritzer resistivity show an evolving plasma conductivity rather than temporally constant as was assumed in the Martin/Braginskii model.

From the electrical measurements it was calculated that the plasma conductivity linearly increases during the rising edge of the current pulse. This further indicates that the assumption of the temporally constant plasma conductivity is not valid for HV-LTSs operating under the

conditions tested (in a transient dominated regime). In addition to the changing plasma conductivity, the Spitzer resistivity model does not accurately predict the plasma channel resistivity for the conditions tested in this work. The likely cause of the overestimation for resistance by the Spitzer resistivity model is due to the low (incomplete) ionization level of the studied switch plasma channel.

In conclusion, HV-LTSs operating in a regime dominated transient effects in the current pulse (switch turn-on-time is same order of magnitude as pulse width) may not be accurately modeled with the Martin/Braginskii model due to a non-temporally constant plasma conductivity. Future work should be conducted at a range of operating conditions to determine if this discrepancy between the Martin/Braginskii model assumptions and measured switch operation are specific to the switch operating conditions in this thesis or rather if it is indicative or a broader gap within the model. These additional conditions should include operation at elevated pressures, different working gases, and a range of electric potentials to operate the switch under conditions closer to those used during its application in pulsed power experiments. In addition to further experimentation with the current switch model, further work should be conducted to determine the fundamental cause of the breakdown of the Martin/Braginskii model. These studies should include a range of working gasses, spark gap distances, primary storage mechanisms, and experimental loads.

BIBLIOGRAPY

[1] Carey, W. J., and Mayes, J. R. Marx Generator Design and Performance. Presented at the Conference Record of the Twenty-Fifth International Power Modulator Symposium and

2002 High-Voltage Workshop. International Power Modulator Conference, Hollywood, CA, USA, 2002.

[2] Lehr, J. M., Abdalla, M. D., Burger, J. W., Elizondo, J. M., Fockler, J., Gruner, F., Skipper, M. C., Smith, I. D., and Prather, W. D. Design and Development of a 1 MV, Compact, Self Break Switch for High Repetition Rate Operation. In *12th International Pulsed Power Conference*, No. 2, Monterey, CA, USA, 1999, pp. 1199–1202.

[3] Martin, T. H., Seamen, J. F., and Jobe, D. O. ENERGY LOSSES IN SWITCHES. Presented at the Ninth IEEE International Pulsed Power Conference, Albuquerque, NM, USA, 1993.

[4] Song, F., Li, F., Zhang, B., Zhu, M., Li, C., Wang, G., Gong, H., Gan, Y., Jin, X., Novac, B. M., and Smith, I. R. "A Compact and Repetitively Triggered, Field-Distortion Low-Jitter Spark-Gap Switch." *IEEE Transactions on Plasma Science*, Vol. 47, No. 8, 2019, pp. 4105–4113. https://doi.org/10.1109/TPS.2019.2926617.

[5] Pashaie, B., Schaefer, G., Schoenbach, K. H., and Williams, P. F. "Field-enhancement Calculations for a Field-distortion Triggered Spark Gap." *Journal of Applied Physics*, Vol. 61, No. 2, 1987, pp. 790–792. https://doi.org/10.1063/1.338182.

[6] Peterkin, F. E., and Williams, P. F. "Physical Mechanism of Triggering in Trigatron Spark Gaps." *Applied Physics Letters*, Vol. 53, No. 3, 1988, pp. 182–184. https://doi.org/10.1063/1.100168.

[7] Guenther, A. H., and Bettis, J. R. "The Laser Triggering of High-Voltage Switches." *Journal of Physics D: Applied Physics*, Vol. 11, No. 12, 1978, pp. 1577–1613. https://doi.org/10.1088/0022-3727/11/12/001.

[8] Woodworth, J. R., Frost, C. A., and Green, T. A. "Uv Laser Triggering of High-voltage Gas Switches." *J. Appl. Phys.*, Vol. 53, 1982, p. 7.

[9] Kushner, M. J., Kimura, W. D., and Byron, S. R. "Arc Resistance of Laser-triggered Spark Gaps." *Journal of Applied Physics*, Vol. 58, No. 5, 1985, pp. 1744–1751. https://doi.org/10.1063/1.336023.

[10] Pendleton, W. K., and Guenther, A. H. "Investigation of a Laser Triggered Spark Gap." *Review of Scientific Instruments*, Vol. 36, No. 11, 1965, pp. 1546–1550. https://doi.org/10.1063/1.1719388.

[11] Gottfried, J., Rose, C. E., and Yalin, A. P. Optical and Electrical Diagnostics of a High-Voltage Laser-Triggered Switch with Variable Impedance Load. Presented at the AIAA SCITECH 2023 Forum, National Harbor, MD & Online, 2023.

[12] Larsson, A., Yap, D., Au, J., and Carlsson, T. E. “Laser Triggering of Spark Gap Switches.” *IEEE Transactions on Plasma Science*, Vol. 42, No. 10, 2014, pp. 2943–2947. https://doi.org/10.1109/TPS.2013.2297161.

[13] Wolford, M. F., Myers, M. C., Hegeler, F., and Sethian, J. D. “Dynamics of Laser Triggered, Gas-Insulated Spark Gaps During Repetitive Operation.” *IEEE Transactions on Plasma Science*, Vol. 44, No. 10, 2016, pp. 2410–2423. https://doi.org/10.1109/TPS.2016.2606249.

[14] Rose, C. E. “DEVELOPMENT OF A HIGH-VOLTAGE LASER TRIGGERED SWITCH FACILITY INCLUDING INITIAL OPTICAL AND ELECTRICAL DIAGNOSTICS.” *M.Sc. Thesis, Mechanical Engineering Dept., Colorado State University, Fort Collins, CO*, 2019, p. 69.

[15] Simpson, S., Johns, O., Rose, C., Leckbee, J., Dumitrache, C., Nielsen, D., Yalin, A., and Kiefer, M. “Triggering of a High Pressure Air-Filled High Voltage Spark Gap Switch Using Fiber-Delivered Laser Induced Plasmas Resulting in Sub-Nanosecond Jitter at Low Percentages of Self-Break.” *IEEE Pulsed Power Conference*, Vol. Brighton, United Kingdom, 2017, p. 25.

[16] LeChien, K., Savage, M., Anaya, V., Bliss, D., Clark, W., Corley, J., Feltz, G., Garrity, J., Guthrie, D., Hodge, K., Maenchen, J., Maier, R., Prestwich, K., Struve, K., Stygar, W., Thompson, T., Van Den Avyle, J., Wakeland, P., Wallace, Z., and Woodworth, J. “Development of a 5.4 MV Laser Triggered Gas Switch for Multimodule, Multimegampere Pulsed Power Drivers.” *Physical Review Special Topics - Accelerators and Beams*, Vol. 11, No. 6, 2008, p. 060402. https://doi.org/10.1103/PhysRevSTAB.11.060402.

[17] Guenther, A., and Bettis, J. “12.2 - Laser-Triggered Megavolt Switching.” *IEEE Journal of Quantum Electronics*, Vol. 3, No. 11, 1967, pp. 581–588. https://doi.org/10.1109/JQE.1967.1074398.

[18] Hutsel, B. T., Davis, J.-P., Campbell, R. B., Fowler, W. E., Hanshaw, H. L., Jennings, C., Jones, M., Lemke, R. W., Long, F. W., Lopez, M. R., McKee, G. R., Moore, J. K., Porter, J. L., Savage, M. E., Sceiford, M. E., Stygar, W. A., Corcoran, P. A., Whitney, B. A., Camacho, A. R., Hinshelwood, D., and Wagoner, T. C. Z Machine Circuit Model Development. Presented at the 2013 IEEE 40th International Conference on Plasma Sciences (ICOPS), San Francisco, CA, USA, 2013.

[19] Glover, S. F., Alexander, J. A., Reed, K. W., Pena, G. E., Horry, M. L., Usher, J. M., and Lehr, J. M. “LASER TRIGGERING OF SPARK GAP SWITCHES WITH LESS THAN 100μJ’s OF ENERGY.” *Sandia National Laboratories*, p. 5.

[20] Welch, D. R., Rose, D. V., Thoma, C., Clark, R. E., Miller, C., Madrid, E. A., Zimmerman, W. R., Rambo, P. K., Schwarz, J., Savage, M., and Atherton, B. W. “Kinetic Simulation Studies of Laser-Triggering in the Z Gas Switch.” *Physics of Plasmas*, Vol. 20, No. 8, 2013, p. 083108. https://doi.org/10.1063/1.4818146.

[21] Gottfried, J. A., Roux, M., and Yalin, A. P. “Electron Density and Temperature Measurements by Thomson Scattering in a High-Voltage Laser-Triggered Switch.” *AIAA Aviation 2022 Forum*, 2022, p. 14. https://doi.org/10.2514/6.2022-3496.

[22] Rose, C., Patel, S. G., Simpson, S., and Yalin, A. P. Preliminary Schlieren and Optical Emission Diagnostics of a High-Voltage Laser Triggered Switch. Presented at the AIAA Aviation 2019 Forum, Dallas, Texas, 2019.

[23] Raizer, Y. *Gas Discharge Physics*. Springer Berlin, Heidelberg, 1991.

[24] Dzierże˛ga, K., Mendys, A., and Pokrzywka, B. “What Can We Learn about Laser-Induced Plasmas from Thomson Scattering Experiments.” *Spectrochimica Acta Part B: Atomic Spectroscopy*, Vol. 98, 2014, pp. 76–86. https://doi.org/10.1016/j.sab.2014.03.010.

[25] Bridges, J. M., Cromer, C. L., and McIlrath, T. J. “Investigation of a Laser-Produced Plasma VUV Light Source.” *Applied Optics*, Vol. 25, No. 13, 1986, p. 2208. https://doi.org/10.1364/AO.25.002208.

[26] Boeuf, J. P. “Plasma Display Panels: Physics, Recent Developments and Key Issues.” *Journal of Physics D: Applied Physics*, Vol. 36, No. 6, 2003, pp. R53–R79. https://doi.org/10.1088/0022-3727/36/6/201.

[27] Weber, L. F. “History of the Plasma Display Panel.” *IEEE Transactions on Plasma Science*, Vol. 34, No. 2, 2006, pp. 268–278. https://doi.org/10.1109/TPS.2006.872440.

[28] Chu, P. K., Qin, S., Chan, C., Cheung, N. W., and Larson, L. A. “Plasma Immersion Ion Implantation—a Fledgling Technique for Semiconductor Processing.” *Materials Science and Engineering: R: Reports*, Vol. 17, Nos. 6–7, 1996, pp. 207–280. https://doi.org/10.1016/S0927-796X(96)00194-5.

[29] Kelly, P. J., and Arnell, R. D. “Magnetron Sputtering: A Review of Recent Developments and Applications.” *Vacuum*, Vol. 56, No. 3, 2000, pp. 159–172. https://doi.org/10.1016/S0042-207X(99)00189-X.

[30] Goebel, D. M., and Katz, I. “Fundamentals of Electric Propulsion: Ion and Hall Thrusters.” p. 493.

[31] Gottfried, J., Antozzi, S., Dumitrache, C., and Yalin, A. P. Preliminary Krypton Measurements by Two-Photon Absorption Laser Induced Fluorescence (TALIF) in Cold Flow and a Hollow Cathode Plasma. Presented at the AIAA SCITECH 2023 Forum, National Harbor, MD & Online, 2023.

[32] Barbarino, M. “A Brief History of Nuclear Fusion.” *Nature Physics*, Vol. 16, No. 9, 2020, pp. 890–893. https://doi.org/10.1038/s41567-020-0940-7.

[33] Chen, F. F. *Introduction to Plasma Physics and Controlled Fusion*. Springer International Publishing, Cham, 2016.

[34] Lieberman, M. A., and Lichtenberg, A. J. *Principles of Plasma Discharges and Materials Processing: Lieberman/Plasma 2e*. John Wiley & Sons, Inc., Hoboken, NJ, USA, 2005.

[35] Lieberman, M. A., and Lichtenberg, A. *Principles of Plasma Discharges and Materials Processing*. John Wiley & Sons, 2005.

[36] Spitzer, L., and Härm, R. "Transport Phenomena in a Completely Ionized Gas." *Physical Review*, Vol. 89, No. 5, 1953, pp. 977–981. https://doi.org/10.1103/PhysRev.89.977.

[37] Shah, S. I. W. "VARIATION OF PLASMA RESISTIVITY DURING TOKAMAK START-UP." p. 7.

[38] Honda, M. "Coulomb Logarithm Formulae for Collisions between Species with Different Temperatures." *Japanese Journal of Applied Physics*, Vol. 52, No. 10R, 2013, p. 108002. https://doi.org/10.7567/JJAP.52.108002.

[39] Weber, R. E., and Tempelmeyer, K. E. *CALCULATION OF THE D-C ELECTRICAL CONDUCTIVITY OF EQUILIBRIUM NITROGEN AND ARGON PLASMA WITH AND WITHOUT ALKALI METAL SEED:* Defense Technical Information Center, Fort Belvoir, VA, 1964.

[40] Cohen, R. S., Spitzer, L., and Routly, P. McR. "The Electrical Conductivity of an Ionized Gas." *Physical Review*, Vol. 80, No. 2, 1950, pp. 230–238. https://doi.org/10.1103/PhysRev.80.230.

[41] Trintchouk, F., Yamada, M., Ji, H., Kulsrud, R., and Carter, T. "Measurement of the Transverse Spitzer Resistivity during Collisional Magnetic Reconnection." *Princeton Plasma Physics Laboratory*, 2002.

[42] Braginskii, S. "Theory of the Development of a Spark Chennel." *J. Exptl. Throret. Phys.*, Vol. 34, Nos. 1548–1557, 1958.

[43] Montano, R., Becerra, M., Cooray, V., Rahman, M., and Liyanage, P. "Resistance of Spark Channels." *IEEE Transactions on Plasma Science*, Vol. 34, No. 5, 2006, pp. 1610–1619. https://doi.org/10.1109/TPS.2006.883350.

[44] Gottfried, J., Rose, C., Simpson, S., and Yalin, A. "Collective Thomson Scattering Measurement of Plasma Evolution During the Current Pulse in a Laser-Triggered Switch." *Applied Physics Letters*, 2022. https://doi.org/DOI: 10.1063/5.0131471.

[45] Lavrinovich, I. V., and Oreshkin, V. I. "Numerical Simulation and Analysis of Energy Loss in a Nanosecond Spark Gap Switch." *Journal of Physics: Conference Series*, Vol. 552, 2014, p. 012021. https://doi.org/10.1088/1742-6596/552/1/012021.

[46] Hanson, R. K., Goldenstein, C. S., and Spearrin, R. M. *Spectroscopy and Optical Diagnostics for Gases*. Springer International Publishing : Imprint: Springer, Cham, 2016.

[47] Eckbreth, A. C. *Laser Diagnostics for Combustion Temperature and Species*. Gordon and Breach Publishers, 1996.

[48] Sande, M. van de, and Sande, M. J. van de. *Laser Scattering on Low Temperature Plasmas: High Resolution and Stray Light Rejection*. 2002.

[49] Peacock, N. J., Robinson, D. C., Forrest, M. J., Wilcock, P. D., and Sannikov, V. V. "Measurement of the Electron Temperature by Thomson Scattering in Tokamak T3." *Nature*, Vol. 224, No. 5218, 1969, pp. 488–490. https://doi.org/10.1038/224488a0.

[50] Uchino, K., Muraoka, T., Muraoka, K., and Akazaki, M. "Studies of an Impulse Breakdown Process in an Atmospheric Air Using Ruby-Laser Scattering Diagnostics." *Japanese Journal of Applied Physics*, Vol. 21, No. Part 2, No. 11, 1982, pp. L696–L698. https://doi.org/10.1143/JJAP.21.L696.

[51] Uchino, K., Itsumi, Y., Muraoka, K., and Akazaki, M. "Ruby-Laser Scattering Diagnostics of DC-Arcs in Atmospheric Air." *Japanese Journal of Applied Physics*, Vol. 23, No. Part 1, No. 5, 1984, pp. 662–662. https://doi.org/10.1143/JJAP.23.662.

[52] Muraoka, K., and Kono, A. "Laser Thomson Scattering for Low-Temperature Plasmas." *Journal of Physics D: Applied Physics*, Vol. 44, No. 4, 2011, p. 043001. https://doi.org/10.1088/0022-3727/44/4/043001.

[53] Murray, C. S. "Evolution of Electron Properties After Nanosecond Repetitively Pulsed Discharges in Air Measured by Thomson Scattering." *M.Sc. Thesis, Physics Dept., Wright State University, Dayton, OH*, 2020, p. 68.

[54] Friss, A. J. "CAVITY ENHANCED THOMSON SCATTERING FOR PLASMA DIAGNOSTICS." *Ph.D. Dissertation, Mechanical Engineering Dept., Colorado State University, Fort Collins, CO*, 2019, p. 183.

[55] Vincent, B., Tsikata, S., Mazouffre, S., Minea, T., and Fils, J. "A Compact New Incoherent Thomson Scattering Diagnostic for Low-Temperature Plasma Studies." *Plasma Sources Science and Technology*, Vol. 27, No. 5, 2018, p. 055002. https://doi.org/10.1088/1361-6595/aabd13.

[56] He, Z., Smith, C., Zhang, Z., Biewer, T. M., Jiang, N., Hsu, P. S., and Roy, S. "Pulse-Burst Laser-Based 10 KHz Thomson Scattering Measurements." *Plasma Science and Technology*, Vol. 21, No. 10, 2019, p. 105603. https://doi.org/10.1088/2058-6272/ab2e30.

[57] Hutchinson, I. H. *Principles of Plasma Diagnostics*. Cambridge University Press, 2002.

[58] Huang, M., Yang, P. Y., Hanselman, D. S., Monnig, C. A., and Hieftje, G. M. "Verification of a Maxwellian Electron-Energy Distribution in the ICP." *Spectrochimica Acta Part B: Atomic Spectroscopy*, Vol. 45, Nos. 4–5, 1990, pp. 511–520. https://doi.org/10.1016/0584-8547(90)80126-4.

[59] Salpeter, E. E. "Electron Density Fluctuations in a Plasma." *Physical Review*, Vol. 120, 1960, pp. 1528–1535. https://doi.org/doi:10.1103/physrev.120.1528.

[60] Warner, K., and Hieftje, G. M. "Thomson Scattering from Analytical Plasmas." *Spectrochimica Acta Part B: Atomic Spectroscopy*, Vol. 57, No. 2, 2002, pp. 201–241. https://doi.org/10.1016/S0584-8547(01)00372-X.

[61] Fried, B. D., and Conte, S. D. TABLE GENERATION AND ACCURACY. In *The Plasma Dispersion Function*, Elsevier, 1961, pp. 5–7.

[62] McNab, I. R. "Large-Scale Pulsed Power Opportunities and Challenges." *IEEE Transactions on Plasma Science*, Vol. 42, No. 5, 2014, pp. 1118–1127. https://doi.org/10.1109/TPS.2014.2303884.

[63] Hogg, M. G., Timoshkin, I. V., MacGregor, S. J., Wilson, M. P., Given, M. J., and Wang, T. Electrical Breakdown of Short Non-Uniform Air Gaps. Presented at the 2013 IEEE Pulsed Power and Plasma Science Conference (PPPS 2013), San Francisco, CA, USA, 2013.

[64] Dzierżęga, K., Mendys, A., Pellerin, S., Thouin, E., Travaille, G., Bousquet, B., Canioni, L., and Pokrzywka, B. "Thomson Scattering from Laser Induced Plasma in Air." *Journal of Physics: Conference Series*, Vol. 227, 2010, p. 012029. https://doi.org/10.1088/1742-6596/227/1/012029.

[65] Beverly, R. E., and Campbell, R. N. "Aqueous-electrolyte Resistors for Pulsed Power Applications." *Review of Scientific Instruments*, Vol. 66, No. 12, 1995, pp. 5625–5629. https://doi.org/10.1063/1.1146029.

[66] Dzierżęga, K., Mendys, A., Pellerin, S., Thouin, E., Travaille, G., Bousquet, B., Canioni, L., and Pokrzywka, B. "Thomson Scattering from Laser Induced Plasma in Air." 2010.

[67] Tomita, K., Kagawa, T., Uchino, K., Katsuki, S., and Akiyama, H. "Collective Thomson Scattering Diagnostics of EUV Plasmas." 2009, p. 5.

[68] Hatae, T., Nagashima, A., Kondoh, T., Kitamura, S., Kashiwabara, T., Yoshida, H., Naito, O., Shimizu, K., Yamashita, O., and Sakuma, T. "YAG Laser Thomson Scattering Diagnostic on the JT-60U." *Review of Scientific Instruments*, Vol. 70, No. 1, 1999, pp. 772–775. https://doi.org/10.1063/1.1149392.

[69] Sato, Y., Tomita, K., Tsukiyama, S., Eguchi, T., Uchino, K., Kouge, K., Tomuro, H., Yanagida, T., Wada, Y., Kunishima, M., Kodama, T., and Mizoguchi, H. "Spatial Profiles of Electron Density, Electron Temperature, Average Ionic Charge, and EUV Emission of Laser-

Produced Sn Plasmas for EUV Lithography." *Japanese Journal of Applied Physics*, Vol. 56, No. 3, 2017, p. 036201. https://doi.org/10.7567/JJAP.56.036201.

[70] Mendys, A., Kański, M., Farah-Sougueh, A., Pellerin, S., Pokrzywka, B., and Dzierżęga, K. "Investigation of the Local Thermodynamic Equilibrium of Laser-Induced Aluminum Plasma by Thomson Scattering Technique." *Spectrochimica Acta Part B: Atomic Spectroscopy*, Vol. 96, 2014, pp. 61–68. https://doi.org/10.1016/j.sab.2014.03.009.

[71] Suttle, L. G., Hare, J. D., Halliday, J. W. D., Merlini, S., Russell, D. R., Tubman, E. R., Valenzuela-Villaseca, V., Rozmus, W., Bruulsema, C., and Lebedev, S. V. "Collective Optical Thomson Scattering in Pulsed-Power Driven High Energy Density Physics Experiments (Invited)." *Review of Scientific Instruments*, Vol. 92, No. 3, 2021, p. 033542. https://doi.org/10.1063/5.0041118.

[72] Linss, V., Kupfer, H., Peter, S., and Richter, F. "Two N_2^+ ($B^2{}_u^+$) Populations with Different Boltzmann Distribution of the Rotational Levels Found in Different Types of N_2 /Ar Discharges—Improved Estimation of the Neutral Gas Temperature." *Journal of Physics D: Applied Physics*, Vol. 37, No. 14, 2004, pp. 1935–1944. https://doi.org/10.1088/0022-3727/37/14/008.

[73] Cristoforetti, G., De Giacomo, A., Dell'Aglio, M., Legnaioli, S., Tognoni, E., Palleschi, V., and Omenetto, N. "Local Thermodynamic Equilibrium in Laser-Induced Breakdown Spectroscopy: Beyond the McWhirter Criterion." *Spectrochimica Acta Part B: Atomic Spectroscopy*, Vol. 65, No. 1, 2010, pp. 86–95. https://doi.org/10.1016/j.sab.2009.11.005.

[74] Savage, M. Pulsed Power Electrical Diagnostics Techniques and Analysis. IEEE Pulsed Power-Plasma Science Mini-course, Jun 23, 2007.

[75] Petrova, Tz. B., Ladouceur, H. D., and Baronavski, A. P. "Nonequilibrium Dynamics of Laser-Generated Plasma Channels." *Physics of Plasmas*, Vol. 15, No. 5, 2008, p. 053501. https://doi.org/10.1063/1.2907787.

[76] Summers, H. P., and McWhirter, R. W. P. "Radiative Power Loss from Laboratory and Astrophysical Plasmas. I. Power Loss from Plasmas in Steady-State Ionisation Balance." *Journal of Physics B: Atomic and Molecular Physics*, Vol. 12, No. 14, 1979, pp. 2387–2412. https://doi.org/10.1088/0022-3700/12/14/022.

[77] Borg, G. G., Harris, J. H., Martin, N. M., Thorncraft, D., Milliken, R., Miljak, D. G., Kwan, B., Ng, T., and Kircher, J. "Plasmas as Antennas: Theory, Experiment and Applications." *Physics of Plasmas*, Vol. 7, No. 5, 2000, pp. 2198–2202. https://doi.org/10.1063/1.874041.

APPENDIX A: COMPARISON OF SHORT CIRCUIT AND RESISTIVE LOAD

In previous studies described in section 1-dd, the HV-LTS was operated with a short-circuit configuration. This was updated to use a resistive load as it produced characteristics closer to those in pulsed power experiments. The main concern was that the strong reflections in current flow were modifying the plasma characteristics to the point that diagnostic measurements would no longer provide insight into the assumptions of the Martin/Braginskii model. Prior to changing the HV-LTS circuit, laser Thomson measurements were recorded up to delay times of 500 ns. As seen in figure 2-6, the short circuit current remains at a large amplitude at 500 ns and later. Figures A-1 and A-2 are the comparison of the HV-LTS plasma electron temperature and density from Thomson scattering for the short circuit and resistive load electrical configurations.

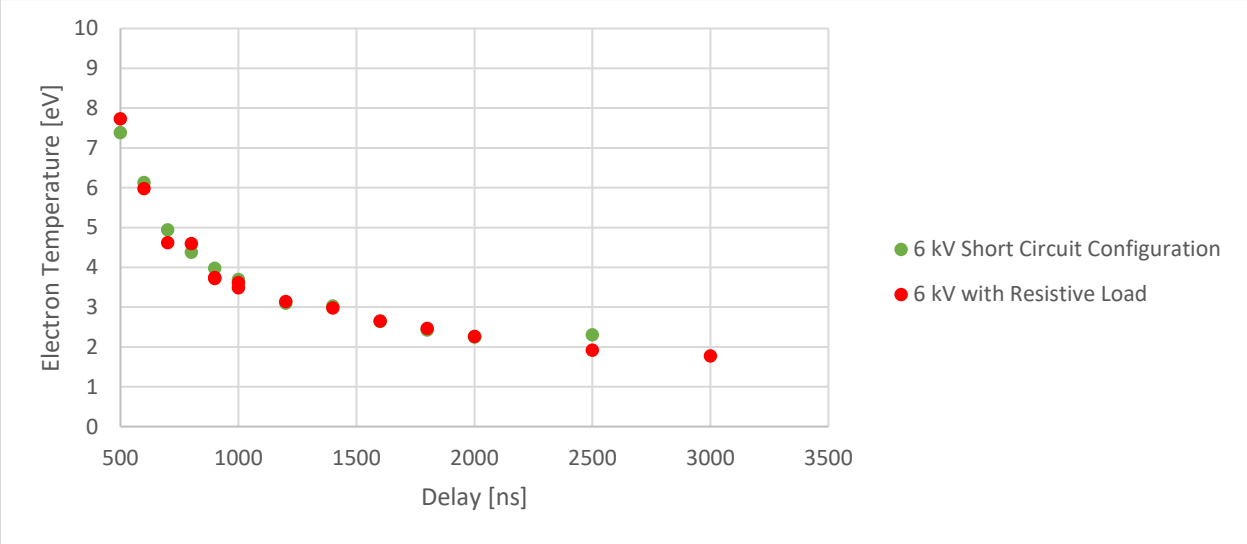

Figure A-1 Comparison of plasma channel electron temperature for the short circuit and resistive load circuits where the main capacitor is charged to 6 kV

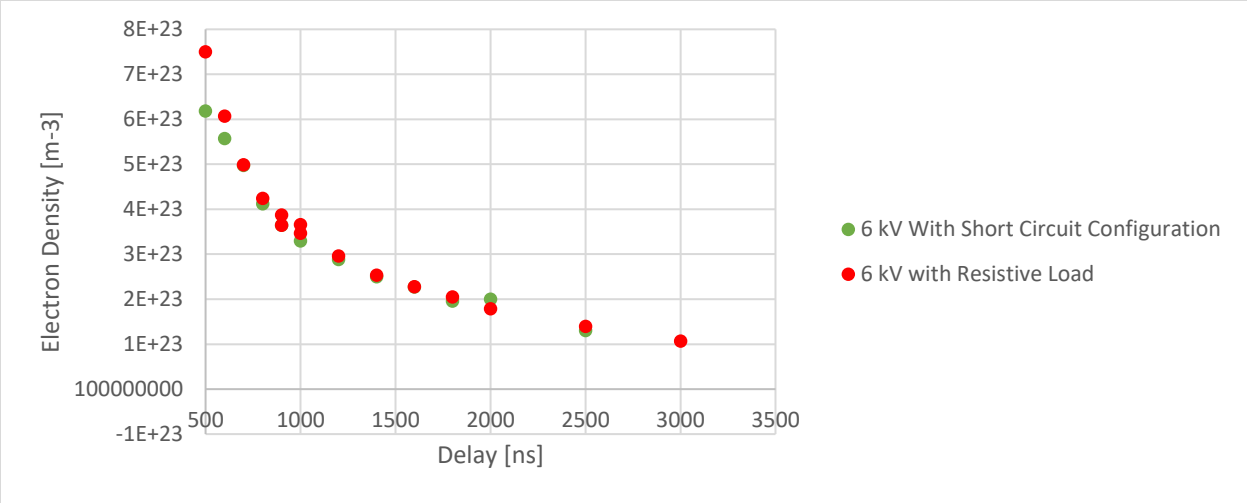

Figure A-2 Comparison of plasma channel electron density for the short circuit and resistive load circuits where the main capacitor is charged to 6 kV

There is no noticeable difference between the electron temperature and density for the short circuit and resistive load cases for delay times greater than 500 ns. This result directly contradicts the assumption of the plasma being reheated by reflections in the current (which in effect causes current flow through the plasma for an extended period. More importantly, during this time frame, there is no current flow for the resistive load case while the current flow in the short circuit is near its maximum value. This leads to the assumption that the heating of the plasma is dominated by the characteristics of the initial rising edge of the current pulse (or first rising edge in the short circuit). Although it presents minimal value to the models or use cases of HV-LTSs, an investigation and further comparison between the short circuit and resistive load configurations should be completed to better understand the plasma physics leading to this result.